Universidade de Brasília – UnB

Faculdade UnB Gama – FGA

Engenharia Aeroespacial

Numerical analysis of regenerative cooling of a 3D-printed hybrid rocket engine.

Autor: Lucas Vinícius de Souza Nascimento

Orientador: Olexiy Shynkarenko, PhD

Brasília, DF

2024

Lucas Vinícius de Souza Nascimento

Numerical analysis of regenerative cooling of a 3D-printed hybrid rocket engine.

Monografia submetida ao curso de graduação em Engenharia Aeroespacial da Universidade de Brasília, como requisito parcial para obtenção do Título de Bacharel em Engenharia Aeroespacial.

Universidade de Brasília – UnB

Faculdade UnB Gama – FGA

Orientador: Olexiy Shynkarenko, PhD

Brasília, DF

2024

Lucas Vinícius de Souza Nascimento

Numerical analysis of regenerative cooling of a 3D-printed hybrid rocket engine.

Monografia submetida ao curso de graduação em Engenharia Aeroespacial da Universidade de Brasília, como requisito parcial para obtenção do Título de Bacharel em Engenharia Aeroespacial.

Trabalho aprovado. Brasília, DF, 19 de setembro de 2024 :

Olexiy Shynkarenko, PhD
Supervisor

Artur Elias de Morais Bertoldi, PhD
Guest 1

Jungpyo Lee, PhD
Guest 2

Brasília, DF
2024

Agradecimentos

"The best way out is always through."
- *Robert Frost*

Abstract

Hybrid rocket engines, operating at temperatures as high as 3000 K, necessitate robust heat dissipation methods due to exceeding the melting points of commonly used metals. The development of the SARA V3 hybrid rocket motor at the University of Brasilia's Chemical Propulsion Laboratory required an integrated pipe coolant design and thorough thermal analysis.

Computational methods were employed to address the impracticality of experimental validation for every design parameter. The focus was on a single printed cooling channel integrated into a wall. Given the static nature of the test project, water was selected as the coolant for its ease of use.

The thesis is divided into two parts. The primary section establishes flow parameters, creates an initial simulation model with a simplified geometry, and includes a literature review. The second part presents the final simulations, mesh validation, and results analysis.

The project aimed to find the optimal configuration of the water channels, varying the number of channels and their thickness. The results reveal the optimal case.

Key-words: Aerospace engineering. Hybrid rocket motors. Additive manufacturing. Regenerative cooling. Hydrodynamics. Fluid dynamics. Water cooling channels.

Lista de ilustrações

Lista de tabelas

Lista de abreviaturas e siglas

AM   Additive manufacturing

BPF   Blown Powder Deposition

CFD   Computer Fluid Dynamics

CNPq   National Research Council

CPL   Chemical Propulsion Laboratory

DED   Directed Energy Deposition

DMLS   Direct Metal Laser Sintering

EBF3   Electron Beam Free-form Fabrication

EBM   Electron Beam Melting

EBW   Electron Beam Welding

FAPDF   Foundation of the Scientific Support of the Federal District

HDPE   High-Density Polyethylene

LENS   Laser Engineering Net-shaping

LMD   Laser Metal Deposition

LRE   Liquid Rocket Engine

NOX   Nitrous Oxide

PBF   Power Bed Fusion

SLM   Selective Laser Melting

SRM   Solid Rocket Motor

SST   Shear-Stress Transport

TVC   Thurst vectoring Control

WAAM   Wire Arc AM

VCSA   Variable Cross-Sectional Area

Lista de símbolos

$\dot{Q}_{cv}$ Convective heat flux

k Turbulent dissipation

k   Thermal conductivity

m Mass

h_{cv} Convective heat transfer coefficient

S_m Mass source

α_1 Turbulence constant

α_2 Viscosity coefficient

β Turbulence constant

β' Turbulence constant

μ Molecular viscosity

ω Dissipation per unit of turbulent kinetic energy

ρ Specific mass

σ Stefan-Boltzmann constant

σ_k Turbulence constant

σ_ω Turbulence constant

τ Viscous stress

Sumário

1 Introduction

1.1 Motivation and context

To develop a sturdy and long-lasting rocket engine that can undergo consecutive testing and sustain extended burn duration, it is crucial to conduct a comprehensive analysis of thermodynamics, heat transfer, and material properties. Effective heat dissipation techniques must also be implemented to manage the high temperatures generated during operation.

The large amount of energy released by the fuel and oxidizer reaction wields extreme temperature gradients that cause high heat transfer rates, consequent material stress, and possible failure. In addition, combustion temperatures in rocket engines can range from 2700 K to 3600 K (SUTTON; BIBLARZ, 2017), substantially higher than the melting temperature found on commonly used metals such as aluminum. Consequently, a cooling method is needed to extend the engine's lifespan and ensure adequate operation safety standards.

The Chemical Propulsion Laboratory (CPL) has researched hybrid rocket design for years, using the SARA rocket engine generations. Recently, an effective Thrust Vectoring control (TVC) was developed, with the design of a gimble structure and effective linear actuators.

CPL, with financial assistance from the Foundation of the Scientific Support of the Federal District (FAPDF, grant 00193-00001125/2021-33) and the National Research Council (CNPq, grant 405499/2022-1), is now developing a new version (SARA V3) engine. SARA v3 represents the first generation of SARA hybrid engines to be constructed using 3D-printed metal additive manufacturing applied to thermally resistant metal alloys. This advanced technology allows the seamless integration of internal cooling channels within the nozzle structure and cost reduction, making possible effective implementation on low-budget small engines (VEKILOV; LIPOVSKYI; MARCHAN, 2021).

Additive manufacturing, or 3D printing, has revolutionized rocket engine design by enabling the creation of complex geometries and internal structures that were previously impossible or prohibitively expensive to manufacture. This design freedom allows engineers to optimize cooling channels, reduce weight, and consolidate parts, improving performance, reliability, and cost-effectiveness. In the context of SARA v3, additive manufacturing has been instrumental in incorporating intricate cooling channels directly into the nozzle, enhancing heat dissipation and overall engine durability.

The additive manufacturing-driven design also enables rapid iterations of engine

components during the developmental phase. Engineers can quickly produce multiple design versions, test them, and adjust the designs based on feedback, significantly speeding up the development process. The ability to produce parts with internal cooling channels directly as part of the structure, without complex assembly processes, reduces manufacturing time and cost while improving component reliability. Moreover, the capability to print with advanced, heat-resistant alloys such as Inconel allows for enhanced material performance at elevated temperatures, a critical requirement for rocket engine applications where thermal loads are extreme.

Extensive research is being done in the laboratory in many different areas. The present works aim to concentrate on the computational study of a future implementation of regenerative cooling channels on the SARA rocket engine by utilizing CFD analysis, paving the way for the finished project and consequent construction real-life testing. Through this combination of computational and experimental techniques, additive manufacturing-driven design is poised to revolutionize the development and performance of hybrid rocket engines, ensuring not only better thermal management but also enhanced structural integrity and reduced production costs.

1.2 General Goal

Find numerically an optimal cooling channel geometry for a hybrid rocket engine SARA v3 by changing the flow channel design.

The selected design will then undergo numerical simulation using *Ansys* software to evaluate its performance and ensure the engine can withstand minute-scale static tests.

1.3 Specific Goal

- Elaborate a coupled CFD model of the mass and heat transfer inside the combustion chamber of the hybrid rocket engine.

- Develop a mesh that can be used to analyze different cooling channel geometries, varying channel aspect ratios, and channel quantities.

- Ensure that the design can be built using 3D-printed metal technology.

- Ensure resistance of the combustion chamber during 15 seconds of sustained burn.

- Assure simulation integrity through the use of mesh and output parameters.

1.4   Work Structure

This work is organized as follows: The theoretical foundation, including a rocket design overview, SARA design, heat transfer theory, regenerative cooling, and additive manufacturing methods for rocket engines, can be found in section 2. Section 3 details the methodology of the selected finite element method, including mesh, boundary conditions, and setup definitions. Finally, in section 4, results are viewed and discussed, and the optimized geometry is detailed.

2 Theoretical Foundation

2.1 Hybrid Rocket design

Rocket engines are essential in the aerospace industry since they transport structures such as satellites into space. These engines are categorized into liquid, solid, or hybrid types, each utilizing unique technologies.

The hybrid propulsion system emerges as a versatile technology, exemplified in projects like the SARA rocket series found in the CPL Lab. It integrates the advantageous features of both solid and liquid rocket engines to achieve specific performance characteristics. In this configuration, the propulsion system consists of a stationary solid fuel grain and gaseous oxidizers, forming the elements of the hybrid rocket.

The solid fuel grain, typically composed of fuel and binder materials, resides within the combustion chamber. This design choice offers simplicity, stability, and easy storage, unlike traditional solid rocket engines. The solid fuel grain remains stationary throughout the operation.

Contrastingly, the oxidizers, existing in a gaseous state, necessitate a separate feed system to introduce them into the combustion chamber. A pressurized tank stores the oxidizer, forcing it into the combustion chamber at the desired flow rate 1. The oxidizer then mixes with the solid fuel grain, undergoes combustion, and generates the necessary thrust for propulsion.

Figura 1 – Hybrid Rocket Engine Schematic. (BUSSMANN, 2022)

In contrast to solid rocket engines, the solid fuel grain utilized in a hybrid engine remains inert and unable to combust independently. Its ignition depends on the presence of a separate oxidizer, rendering it adjustable and relatively safe. Typically, the solid fuel comprises high-density hydrocarbons like paraffin or other petroleum-derived solids. For instance, in the case of the SARA engine, the fuel is composed of High-Density Polyethylene (HDPE) and paraffin (SHYNKARENKO, 2022).

Kuo e Chiaverini (2007) state various advantages of hybrid rockets as follows:

1. **Safety:** The inert nature of hybrid rocket fuel ensures it can be handled with a high degree of safety. Unlike solid rocket engines (SRMs), the hybrid system is non-

explosive due to the inability to intimately mix the fuel and oxidizer. Consequently, an assembled hybrid system can be stored, transported, and handled with fewer restrictions than SRM.

2. **Simplicity:** One of the key advantages of hybrid rocket systems is their control simplicity. In hybrids, combustion depends on the oxidizer flow within the combustion chamber, permitting the system to be regulated by adjusting the oxidizer flow rate through a valve. This considerably simplifies the process of throttling a hybrid system when compared to a liquid rocket engine (LRE), which necessitates the modulation of two flow rates while ensuring a precise fuel-oxidizer mixture. Additionally, the capacity to modulate the oxidizer flow rate in hybrids facilitates simple system shutdown, offering additional safety and practical advantages.

3. **Propellant versatility:** Hybrid rocket systems provide a broad spectrum of fuel options, offering flexibility in the selection of propellants. Unlike liquid rockets, hybrids can integrate solid additives, including energetic metals, to enhance their performance. Moreover, the liquid oxidizers utilized in hybrid systems generally yield higher specific impulses than solid rockets. This adaptability in propellant choice enables the application of hybrid systems in diverse rocket scenarios, spanning from sounding rockets and tactical missiles to space propulsion. .

4. **Low cost:** Hybrid rocket systems present a cost-saving advantage by combining simplicity, as opposed to liquid rockets, and safety superior to solid rockets. These attributes collectively result in reduced overall operational costs for hybrid systems when compared to their liquid and solid counterparts.

Meanwhile, the hybrid engine also has some drawbacks, as stated by Kuo e Chiaverini (2007) below:

1. **Combustion efficiency:** In hybrid systems, diffusion flames yield a less thorough mixing of fuel and oxidizer than liquid and solid propulsion. According to Kuo e Chiaverini (2007), this results in a slightly higher efficiency loss of around 1-2 percent in hybrid systems compared to their liquid and solid counterparts.

2. **Low regression rate:** Hybrid fuels typically exhibit a reduced regression rate, often leading to thinner fuel grain dimensions. To meet the thrust requirements, it may be necessary to create fuel grains with multiple ports, thereby increasing the grain's surface area. Nevertheless, this can result in a relatively lower bulk density and the potential presence of unburnt fuel slivers. Recent innovations have addressed this limitation by augmenting regression rates.

2.2   SARA engine design and history

The SARA rocket engines are a series of hybrid designs created in the CPL (Chemical Propulsion Laboratory). The current version is a hybrid engine targeting 2kN. It utilizes paraffin in a mixed fuel along with NOX as an oxidizer. This prototype aims to be metal printed in Inconel 718, allowing internal cooling channels to be included in the walls of the chamber and nozzle. The simplified schematics can be found below.
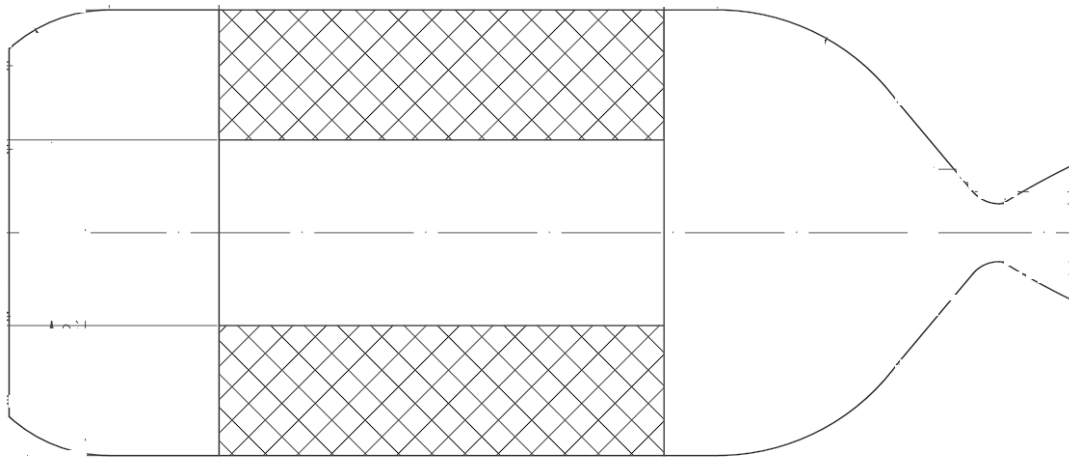
Figura 2 – SARA v3 Hybrid Rocket Engine Schematic. (SHYNKARENKO, 2022)

2.3   Metal Additive Manufacture

Also known as metal 3D printing, Metal Additive manufacturing is an advanced fabrication technique characterized by the layer-by-layer construction of three-dimensional objects using metallic materials. Diverging from conventional subtractive manufacturing methodologies, additive manufacturing involves adding material to create the final product (FRAZIER, 2014).

Key advantages of Metal Additive Manufacturing:

- Complex Geometries: A distinctive advantage of metal additive manufacturing lies in its capacity to fabricate intricate and complex geometries that may be impractical or unattainable through traditional manufacturing processes. This attribute renders the technology particularly advantageous in industries such as aerospace.

- Minimized Material Waste: Unlike conventional manufacturing methods that often result in substantial material wastage during machining or cutting, metal additive

manufacturing exhibits efficiency in material usage by adding material precisely where required, reducing costs.

- Rapid Prototyping and Customization: Metal additive manufacturing is well-suited for rapid prototyping, facilitating swift iterations and modifications during the product development phase, and also facilitating small production scale projects.
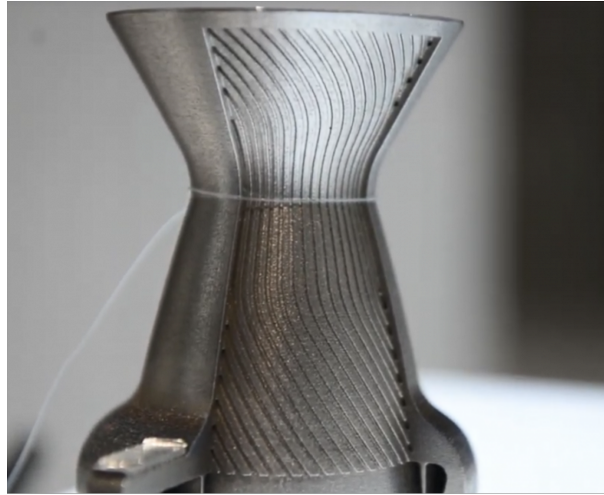
Figura 3 – Example of 3D printed AM rocket nozzle with internal cooling channels (AMFG, 2020)

The two most common AMTs for aerospace applications are DED (Directed energy deposition) and PBF (Powder bed fusion). Widespread DED technologies in the aerospace industry include laser metal deposition (LMD), laser engineering net-shaping (LENS), electron beam welding (EBW), electron beam free-form fabrication (EBF3), and wire arc AM (WAAM)(BOYER; FROES, 2019). In addition, PBF technologies include direct metal laser sintering (DMLS), selective laser melting (SLM), and electron beam melting (EBM). Meanwhile, many different methods of DED and PBF exist, and their working principle always stays the same.

2.3.1   Directed energy deposition

DED technology works by melting material fed to a local site on the build layer, usually occurring within an inert gas atmosphere. While this can be used for nonmetal materials, it is predominately used with metals and metal alloys (BOYER; FROES, 2019). Feedstock usually comes in powder or wire and is melted with a focused energy source, such as laser beams, electron beams, and arcs.DED processes build up the 3D part layer by layer; however, the technology can be implemented in a multiaxial machine and provide 3D positioning. (SING et al., 2020). This allows the manufacturing of complex parts without the need for support structures. Due to increased versatility in orientation, DED

technologies are ideal for the component repair of turbine blades, engine combustion chambers, compressors, and airfoils capable of printing with aerospace-grade materials like Inconel 718 or other alloys.
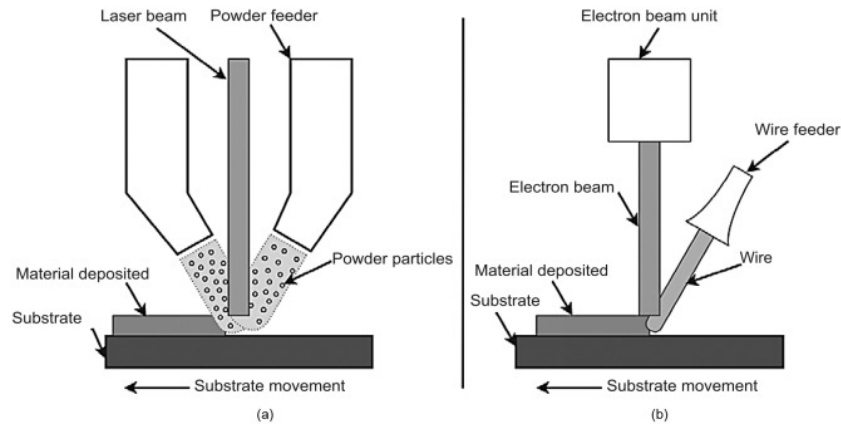
Figura 4 – Directed energy deposition feed by wire and powder (SING et al., 2020)

2.3.2 Powder bed fusion

PBF technologies work by locally melting metal powder on a substrate to form layers. After a new layer is formed, a leveling roller distributes a new layer of powder. Unmelted powder is reusable and supports successive layers, reducing the need for support structures. To avoid powder oxidation, SLM and DMLS occur in an inert gas atmosphere, while EBM occurs in a vacuum (WIBERG, 2019). Consequently, the vacuum requirement makes EBM attractive for outer space manufacturing. Compared to DED processes, PBF processes can create internal passages and, typically, produce higher-fidelity build features.
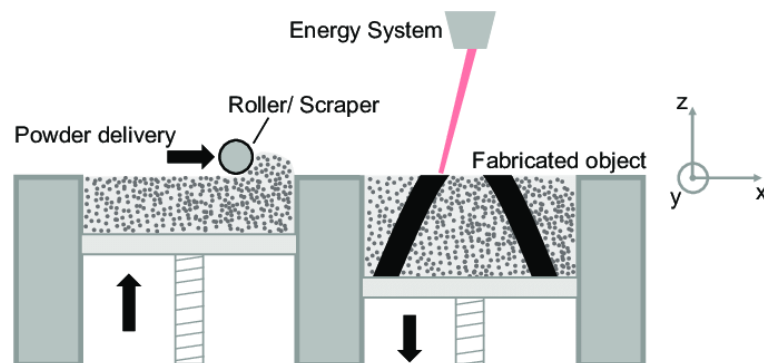
Figura 5 – Powder bed fusion (WIBERG, 2019)

For the present project, the printing method employed is the PBF 5. That choice was made since it was the only method that had a printer available. The explanation of regenerative cooling design applications and examples using AM are located in the following chapters.

2.4   Regenerative cooling design

2.4.1   Traditional methods and application

There are many possible types of rocket nozzle cooling, such as dump, film, transpiration, radiation, ablative, and regenerative cooling (PALATEERDHAM, 2020). However, the most effective and commonly found in real-life applications and studies are the ablative and regenerative cooling methods.

Ablative cooling utilizes a sacrificial material designed to carry heat as it disintegrates and gets transported by the nozzle flow, consequently protecting the metal walls of the structure beneath it. This method shows significant heat endurance performance at low-cost es, especially compared to other methods. However, it shows drawbacks as the dimensions of the internal nozzle walls change during the burn, thus modifying performance parameters (BROWNE, 2020).

Regenerative cooling adds the flow of pressurized propellants on the nozzle surface. This is usually done through pipes placed on the nozzle walls, and they act as heat exchangers by absorbing thermal energy through convection (BROWNE, 2020). This method is usually applied to cryogenic liquid rocket engines since the fuel temperature rises. In addition, the material of the walls acts as a "heatsink"that carries the heat from the internal flow to the cooling lines through conduction. The outstanding performance of this method rendered it the most widely used for cooling rocket engines. However, its implementation is expensive and requires high-level fabrication. An example is the F1 engine, produced by Rocketdyne and used as Saturrn's main engine, the presence of tubes running along the nozzle body was done to implement regenerative cooling through a traditional fabrication method as seen in figure 6.

Figura 6 – F1 engine cooling pipes running through nozzle structure (WIBERG, 2019)

2.4.2 AM's use in regenerative cooling

Rocket Engine components typically include turbopump units, sensors, valves, combustion chambers, etc. However, the combustion chambers often contribute to over 50% of the total engine cost (VEKILOV; LIPOVSKYI; MARCHAN, 2021). This is primarily because the traditional manufacturing of combustion chambers involves intricate processes such as stamping, milling, rotary drawing, brazing, welding techniques, assembly, and post-production heat treatment, all of which require specialized and costly equipment. These processes significantly increase labor intensity and production costs. This cost is further inflated by the implementation of regenerative cooling design, in deterrence of its additional complexity. Figure 7 shows the cost reduction of 3D implementation on low-production projects in contrast to traditional manufacturing.
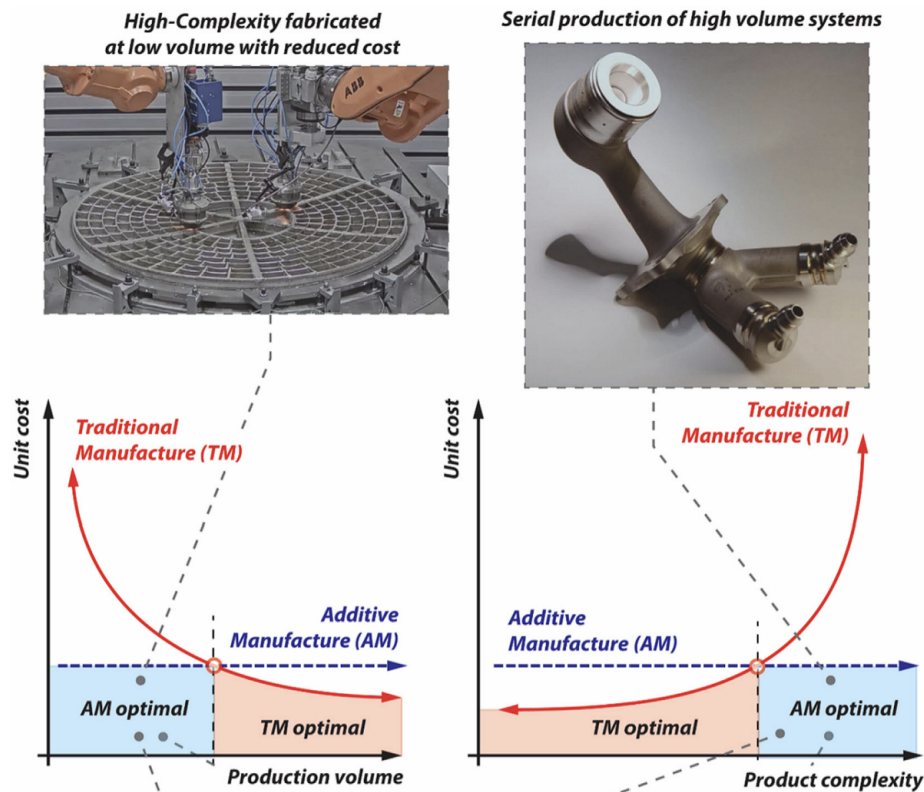
Figura 7 – Cost of manufacturing (BLAKEY-MILNER et al., 2021)

Because of this scenario, a competitive growth of interest in exploring cost-effective solutions to reduce production expenses and enhance efficiency is born (BLAKEY-MILNER et al., 2021). One viable approach is leveraging additive manufacturing technology for producing regenerative cooling channels in combustion chambers and nozzles since they experience thermal loads during operation and often require improved heat transfer from the wall to the coolant. Extensive literature covers applications regarding the implementation of AM in regenerative cooling design.

NASA created a method by the name of blown powder deposition (BPD) (GRADL; PROTZ, 2020). BPT wields a monometallic structure usually made out of Inconel 625. This method produces the engine in a layer-by-layer fashion similar to PBF, forming an integral structure that optimizes heat transfer on its walls while increasing structural performance compared to other methods. However, it is complex to scale up for large nozzle structures, as stated by (GRADL; PROTZ, 2020), leaving it applicable for small-scale projects such as the SARA v3 engine.

Figura 8 – Exemple of NASA's DED powder deposition nozzles (GRADL; PROTZ, 2020)

However, 3D printing has drawbacks, requiring design adaptations due to current printer limitations. These limitations include constraints on angles, surface roughness, and the physical size of structures. Typical minimum printing resolutions feature sizes of approximately 0.2 to 0.4 mm, with a maximum part size of 300–400 mm for most small to medium-sized machines (BLAKEY-MILNER et al., 2021). Figure 9 illustrates the difference between printed layers and the intended geometry, highlighting a typical maximum angle of 45 degrees for unsupported structures.
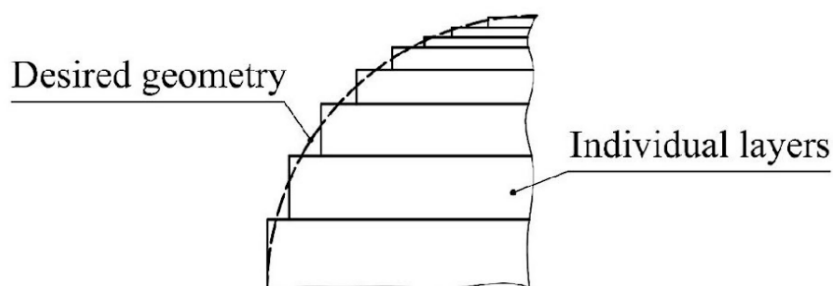
Figura 9 – Step-stair-effect (VEKILOV; LIPOVSKYI; MARCHAN, 2021)

In addition to artificial roughness, modifications can be made to the support walls of the internal channels by altering the number of channels and the aspect ratio (the relationship between the height and width of the channel). These modifications can influence

the pressure of the cooling fluid, causing a drop in pressure during the phase change recurrence, which may be undesirable for regenerative cooling. This is because the pressure lines exiting the cooling channels must meet the correct pressure for correct injection into the combustion chamber later (ULAS; BOYSAN, 2013). However, as the current design for SARA v3 intends to use a separate water loop independent of oxidant injection, the pressure drop can be disregarded. Nevertheless, increasing the number of channels imposes restrictions on the water passage, making it challenging to maintain desirable coolant flow rates.

Furthermore, these modifications affect the heat transfer performance, significantly impacting the wall temperature profile. In a study by (ULAS; BOYSAN, 2013), the author establishes relationships between tube aspect ratios/number of tubes and heat transfer performance. The article indicates that increasing the aspect ratio with a constant number of cooling channels enhances cooling efficiency to an optimum level. After reaching this optimum level, efficiency decreases due to the diminishing heat transfer area, as illustrated in the graph 10.
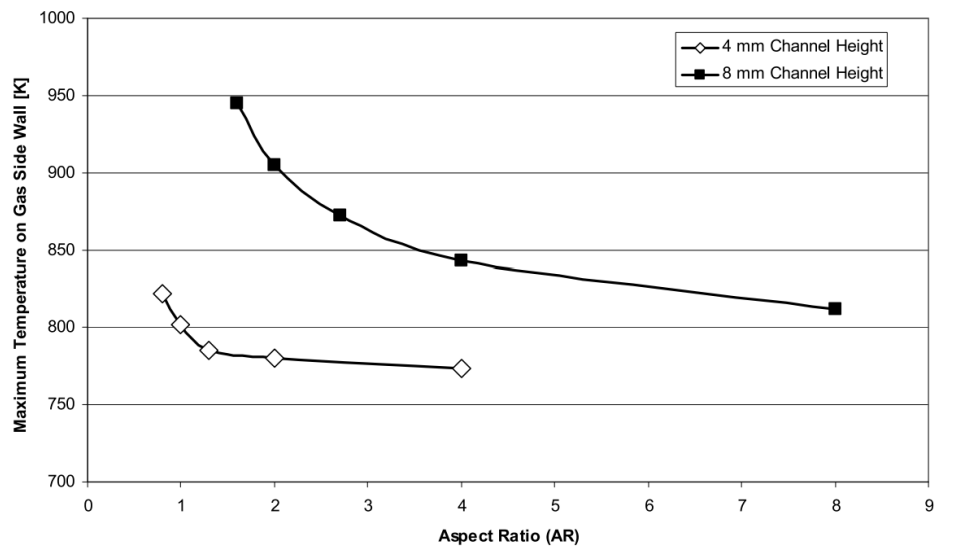
Figura 10 – Effects of aspect ratio on gas side wall temperature (ULAS; BOYSAN, 2013)

In the study by (ULAS; BOYSAN, 2013), it is also mentioned that increasing the number of cooling channels without changing the geometry will enhance cooling efficiency to an optimum level. This is attributed to the dominant effect of increasing the total heat transfer area. However, beyond this optimum level, efficiency decreases due to the dominant effect of decreasing mass flow rate per channel. This phenomenon is depicted in the graph 11.
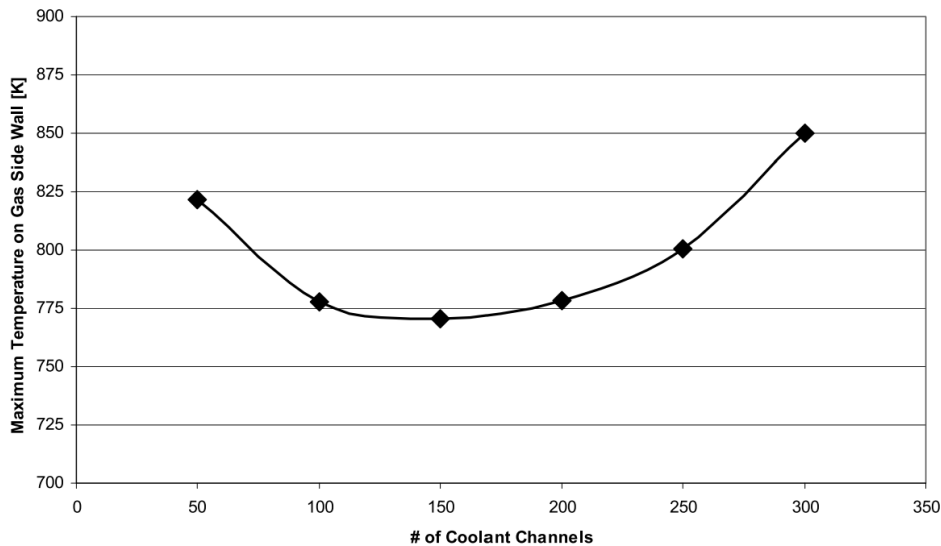
Figura 11 – Effects of the number of channels on gas side wall temperature. (ULAS; BOY-SAN, 2013)

2.5   Thermal heat transfer

The study of heat transfer is crucial for understanding energy flow as heat in systems. It involves estimating heat transfer rates, both in steady and transient states and analyzing temperature distributions. This helps calculate temperature gradients and changes at different locations and times. The fundamental laws governing heat transfer are, according to Kothandaraman (2012):

- The First Law of Thermodynamics, which enforces energy conservation. It relates heat flow, energy storage, and generation in systems, applicable to closed and open systems with minor adjustments.

- The Second Law of Thermodynamics, which dictates that heat energy flows from higher to lower temperature regions or along negative temperature gradients.

- Newton's Laws of Motion determines fluid flow parameters.

- The Law of Conservation of Mass is key in establishing mass flow-related parameters.

- The rate equations as applicable to the particular mode of heat transfer.

Heat transfer modes are primarily dictated by the medium through which heat is transferred and the presence of temperature gradients. In solids, heat predominantly propagates through conduction. When it comes to the interaction between solids and fluids (liquids or gases) or among fluids, heat transfer occurs through convection. In contrast, radiation, a mode of heat transfer, does not rely on a medium; it takes place on the surface of materials with emissivity, involving the emission of photons or electromagnetic waves (ÇENGEL; GHAJAR, 2020).

2.5.1 Conduction

This heat transfer mode relies on temperature differences within or between bodies in thermal contact, with no involvement of mass flow or mixing. Conduction, the predominant method of heat transfer through solid barriers, is extensively encountered in the design of heat transfer equipment and processes like the heating and cooling of various materials, such as heat treatment (ÇENGEL; GHAJAR, 2020). The governing rate equation for conduction is rooted in Fourier's law of heat conduction, which establishes a proportional relationship between heat flow due to conduction, temperature gradients, and the perpendicular surface area. Heat travels in the direction opposite to the temperature gradient, following this law. The proportionality constant within this relationship is recognized as the material's thermal conductivity (k) (KOTHANDARAMAN, 2012). The mathematical expression for this phenomenon is presented in Equation 2.1 along with a visual representation in fig.12:

$$Q = -kA\frac{dT}{dx} \tag{2.1}$$

2.5.2 Convection

This mode of heat transfer is encountered in situations where heat energy is exchanged with a flowing fluid at the surface over which the fluid flows. At its core, this mode involves conduction through an extremely thin fluid layer at the surface, followed by mixing driven by the fluid's motion. Energy transfer occurs through a combination of molecular diffusion and bulk flow. Importantly, the rate of heat transfer is independent of the properties of the material at the surface and is solely dependent on the fluid properties.(ÇENGEL; GHAJAR, 2020). However, the shape and characteristics of the surface significantly influence the flow patterns, thus affecting the heat transfer.

If external mechanisms like fans or pumps induce the flow of the fluid, it is referred to as "forced convection."On the other hand, if the flow arises due to buoyant forces
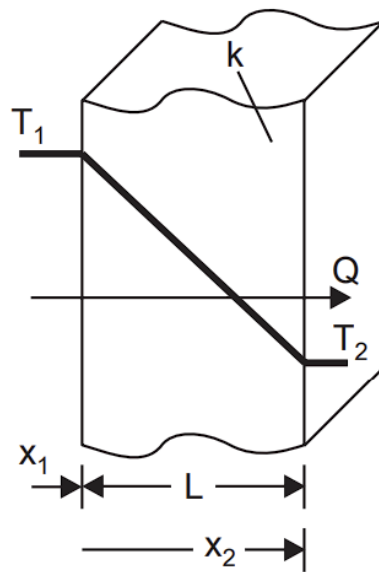
Figura 12 – Conduction physical model, for example. Source:(KOTHANDARAMAN, 2012)

resulting from temperature differences in the fluid body, it is known as "free"or "natural convection."
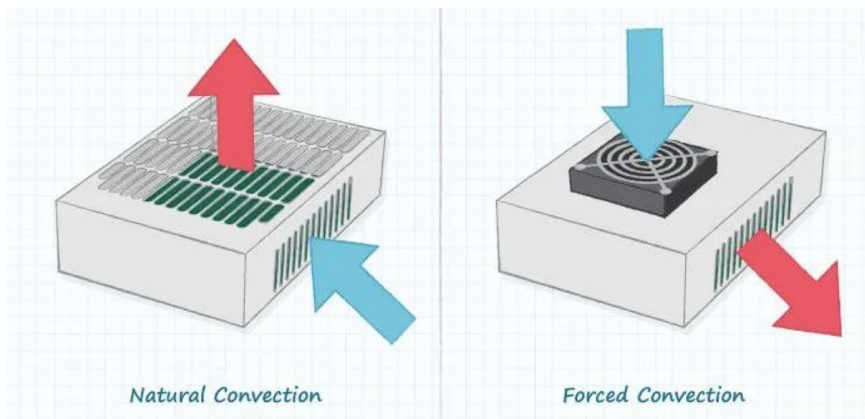
Figura 13 – Example of forced and natural convection. Source:(SMOOT, 2021)

In many practical applications, heat is transferred from one fluid to another, with a solid surface acting as an intermediary. Heat flows from the hot fluid to the surface and from the surface to the colder fluid via convection. In design processes, especially in practical applications, convection is often the most critical heat transfer mode. Newton's contribution was instrumental in this realm, as he consolidated various parameters into a single entity known as the convective heat transfer coefficient (h), as expressed in Equation 2.2.

$$\dot{Q}_{cv} = h_{cv} \cdot ((T_1 - T_2) \tag{2.2}$$

Where $\dot{Q}_{cv}$ is the convective heat flux (W/m²) and is proportional to the temperature difference between the surface (T_1) and the fluid (T_2). The convective heat transfer coefficient (h_{cv}) (W/m²K) depends on boundary layer conditions created by the fluid moving over the surface, surface geometry, flow nature, and various thermodynamic and transport properties of the fluid (KOTHANDARAMAN, 2012).

The physical configuration of this process can be illustrated using a resistance analogy seen in Figure 14.
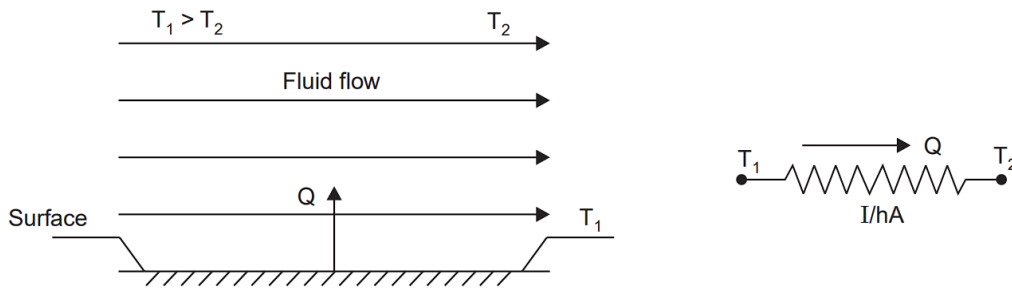
Figura 14 – Electrical analogy for convection heat transfer(KOTHANDARAMAN, 2012)

2.5.3 Radiation

Thermal radiation is a unique mode of heat transfer, operating within the restricted wavelength range of 0.1 to 10 µm on the electromagnetic spectrum. Remarkably, all surfaces emit thermal radiation, regardless of their temperature. This emitted radiation becomes a conduit for heat transfer, facilitating energy exchange between surfaces at varying temperatures. Unlike conduction and convection, radiation doesn't rely on a medium to propagate. Instead, it necessitates direct visual contact between surfaces. The governing law for radiative heat transfer is derived from Stefan-Boltzmann's principle, which underscores that the heat radiated is directly proportional to the fourth power of the absolute temperature of the surface. This principle gives rise to the heat transfer rate equation, as expressed in Equation 2.3.

$$Q = F \cdot \sigma \cdot A \cdot (T_1^4 - T_2^4) \quad (1.4) \qquad\qquad (2.3)$$

In this equation, Q characterizes the heat transfer rate (W), F denotes a factor contingent on surface geometry and properties, σ stands as the Stefan-Boltzmann constant, equal to 5.67×10^{-8} W/m² $\cdot$ K⁴ in SI units, A represents the surface area in square meters (m²), and T_1 and T_2 stand for temperatures measured in Kelvin (K) — the sole acceptable unit for absolute temperature. The interplay of these factors in radiative heat transfer is depicted in Figure 15.
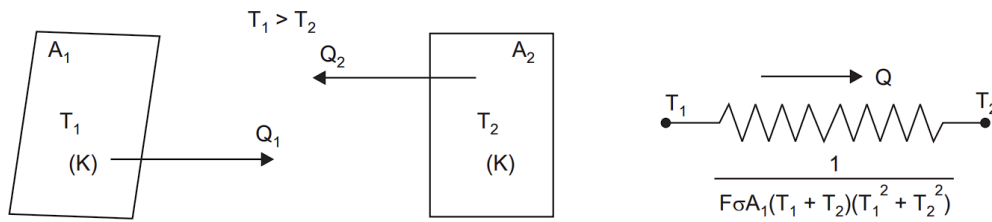
Figura 15 – Radiation between two bodies along with resistance representation of radiation (KOTHANDARAMAN, 2012).

2.6 Computer fluid dynamics

2.6.1 Governing Equations

To comprehend the essence of CFD (Computational Fluid Dynamics)lies in the physical aspects of any fluid flow, which are governed by three fundamental principles: conservation of mass, adherence to Newton's second law (force equals mass times acceleration), and conservation of energy. These fundamental principles can be expressed through basic mathematical equations. Computational Fluid Dynamics represents the art of substituting integral and derivative forms (where applicable) in equations with their discretized algebraic equivalents, which are subsequently solved to yield numerical values for fluid flow at discrete points in both time and space (ANDERSON, 2011).

There are four distinct approaches to constructing a flow model (ANDERSON, 2011). The model utilized in this study to derive mathematical equations employs a fixed control volume in space through which the fluid flows. It's crucial to note that irrespective of the method chosen to derive the equations, the ultimate result will yield a different representation of the same equation, and with appropriate manipulation, any of the other three forms can be derived. With this premise in mind, the mathematical equations will be derived following the procedure outlined in (ANDERSON, 2011).

2.6.1.1 Continuity equation

The continuity equation is one of the fundamental equations in fluid dynamics, and it is integral to the understanding of the subject. The Reynolds Transport Theorem is a key theorem used in these equations. Additionally, the fundamental equations include the conservation of momentum and energy equations.

Consider a finite-sized control volume, which has a general shape and is stationary in space. It is represented by V, as illustrated in 16

Within this volume, there is an infinitesimal volume dV. The control volume is bounded by a surface S (control surface), and at a particular point on this surface, the infinitesimal surface vector dS exists. At the same point, the flow velocity vector V (also
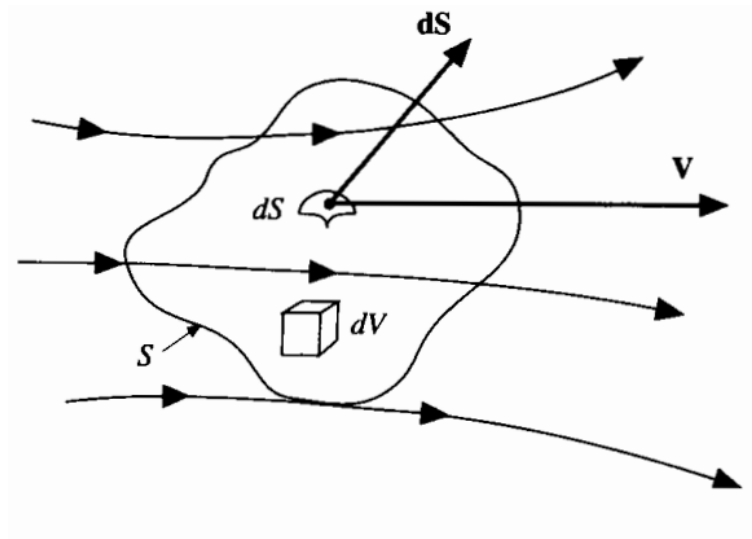
Figura 16 – Fixed control volume (ANDERSON, 2011)

known as U) is also located.

By applying the continuity equation within this control volume, it can be stated that the mass flow leaving the control volume through the surface S is equal to the rate of mass decrease within the control volume V. Equation 4.1 represents this assertion:

$$\rho V_n f dS = \rho V dS \tag{2.4}$$

The mass flow leaving the control volume V is the sum of all flows through the surface S. This summation is represented by an integral and is given by the term $\rho V dS$. Considering the total mass within the control volume V through a triple integral over the infinitesimal control volume (illustrated in Figure 9), we have Equation 4.2:

$$\iint_S (\rho \mathbf{U} \cdot \mathbf{dS}) = \iiint_V \rho dV \tag{2.5}$$

The reduction in mass rate is included on the right side of the previous equation thus:

$$\iint_S (\rho \mathbf{U} \cdot \mathbf{dS}) = -\frac{\partial}{\partial t} \iiint_V \rho dV \tag{2.6}$$

Applying the divergence theorem to obtain volume integral from the surface:

$$\iint_S (\rho \mathbf{U} \cdot \mathbf{dS}) = \iiint_V \nabla \cdot (\rho U) dV \tag{2.7}$$

Inserting equation 2.6 into 2.7:

$$\iiint_V \left[\frac{\partial \rho}{\partial t} + \nabla \cdot (\rho U) \right] dV = 0 \tag{2.8}$$

As V is a known volume, the only way for the integral to be equal to zero is for the value within the brackets to equal zero. Consequently, 2.8: can be simplified to:

$$\frac{\partial \rho}{\partial t} + \nabla \cdot (\rho U) = 0 \tag{2.9}$$

As per ANSYS Inc. (ANSYS, 2011), the equation presented above is the continuity equation applicable to both incompressible and compressible flows. It's expressed in vector form, where the velocity vector U comprises three components corresponding to three-dimensional space. The expansion of the tree components is seen on eq 2.10

$$\frac{\partial \rho}{\partial t} + \frac{\partial}{\partial x}(\rho \nu_x) + \frac{\partial}{\partial y}(\rho \nu_y) + \frac{\partial}{\partial z}(\rho \nu_z) = S_m \tag{2.10}$$

In this context,S_m represents a mass source term introduced into the continuous phase (ANDERSON, 2010).

Starting from the second law of Newton in its generalized form:

$$F = ma = m\frac{\partial U}{\partial t} = \frac{\partial}{\partial t}(mU) \tag{2.11}$$

Where mU represents the momentum of an object with mass m. This equation conveys the physical concept that force equals the rate of change of momentum.
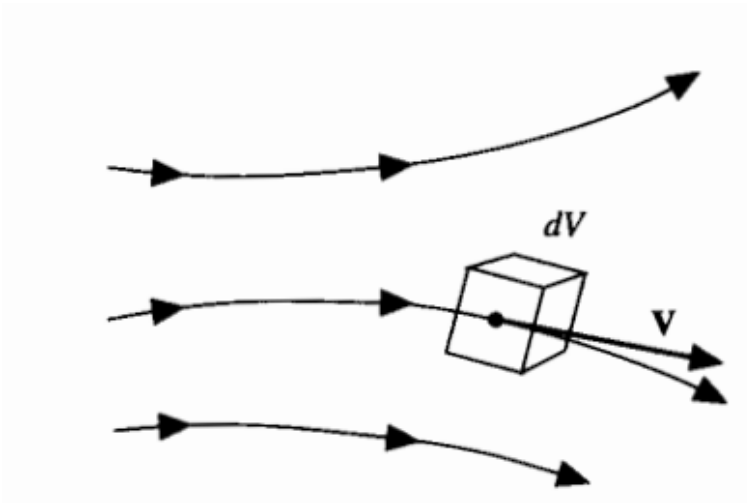
Figura 17 – Infinitesimal control volume moving on a vector field. (ANDERSON, 2011)

Figure 17 represents a control volume moving through space. According to 17 when accompanied by equation 2.11, forces are applied to the infinitesimal body dV. This force can originate from two sources: field forces like gravity and electromagnetic fields and contact forces such as pressure. Denoting F as the total net force per unit mass exerted on the fluid within volume V and dS as the control surface, Equation 4.9 signifies the sum of forces acting on the infinitesimal volume.

$$F = \iiint_V \rho f \, dV - \iint_s p \, dS + F_{Viscoso} \tag{2.12}$$

In Equation 2.12, the rate of change of momentum is the sum of two terms. The first term accounts for the change in net momentum exiting the control volume V through the surface S. The second term pertains to the rate of change of momentum due to fluctuations in fluid properties within volume V. This can be expressed as:

$$\iint_S (\rho \mathbf{U} \cdot \mathbf{dS}) + \frac{\partial}{\partial t} \iiint_V \rho \mathbf{U} \, dV \tag{2.13}$$

Substituting eq. 2.13 and 2.12 in eq. 2.11:

$$\iiint_V \rho \mathbf{f} \, dV - \iint_S p \, \mathbf{dS} + \mathbf{F}_{\text{Viscoso}} = \iint_S (\rho \mathbf{U} \cdot \mathbf{dS}) + \frac{\partial}{\partial t} \iiint_V \rho \mathbf{U} \, dV \tag{2.14}$$

Applying divergence theorem:

$$\iiint_V \left[\frac{\partial(\rho \mathbf{U})}{\partial t} + \nabla \cdot \left(\rho \mathbf{U}^T \mathbf{U} \right) + \nabla \cdot p - \nabla \cdot \tau - \rho \mathbf{f} - (F_x)_{\text{Viscoso}} \right] dV = 0 \tag{2.15}$$

The stress tensor τ 2.16 models viscous stresses exerted on the body surface and are shown on normal and transversal components 2.17.

$$\tau = \begin{bmatrix} \tau_{xx} & \tau_{xy} & \tau_{xz} \\ \tau_{yx} & \tau_{yy} & \tau_{yz} \\ \tau_{zx} & \tau_{zy} & \tau_{zz} \end{bmatrix} \tag{2.16}$$

$$\begin{aligned}
\tau_{xx} &= \lambda(\nabla \cdot \mathbf{U}) + 2\mu \left(\frac{\partial u}{\partial x} \right) & \tau_{xy} = \tau_{yx} &= \mu \left(\frac{\partial u}{\partial y} + \frac{\partial v}{\partial x} \right) \\
\tau_{yy} &= \lambda(\nabla \cdot \mathbf{U}) + 2\mu \left(\frac{\partial v}{\partial y} \right) & \tau_{xz} = \tau_{zx} &= \mu \left(\frac{\partial u}{\partial z} + \frac{\partial w}{\partial x} \right) \\
\tau_{zz} &= \lambda(\nabla \cdot \mathbf{U}) + 2\mu \left(\frac{\partial w}{\partial z} \right) & \tau_{yz} = \tau_{zy} &= \mu \left(\frac{\partial v}{\partial z} + \frac{\partial w}{\partial y} \right)
\end{aligned} \tag{2.17}$$

Where μ is the molecular viscosity and λ the viscosity coeficient (usually considered as $-\frac{2}{3}\mu$. In a similar fashion to continuity equation derivation, the integral of eq 2.15 must be zero. This yields the equations bellow, which state the moment conservation for a 3D space (ANSYS, 2011).

$$\begin{aligned}
\frac{\partial(\rho u)}{\partial t} + \frac{\partial (\rho u^2)}{\partial x} + \frac{\partial(\rho uv)}{\partial y} + \frac{\partial(\rho uw)}{\partial z} &= -\frac{\partial p}{\partial x} + \frac{\partial}{\partial x} \left(\lambda \nabla \cdot \mathbf{V} + 2\mu \frac{\partial u}{\partial x} \right) \\
&+ \frac{\partial}{\partial y} \left[\mu \left(\frac{\partial v}{\partial x} + \frac{\partial u}{\partial y} \right) \right] + \frac{\partial}{\partial z} \left[\mu \left(\frac{\partial u}{\partial z} + \frac{\partial w}{\partial x} \right) \right] + \rho f_x
\end{aligned} \tag{2.18}$$

$$\frac{\partial(\rho v)}{\partial t} + \frac{\partial(\rho uv)}{\partial x} + \frac{\partial\left(\rho v^2\right)}{\partial y} + \frac{\partial(\rho vw)}{\partial z} = -\frac{\partial p}{\partial y} + \frac{\partial}{\partial x}\left[\mu\left(\frac{\partial\nu}{\partial x} + \frac{\partial u}{\partial y}\right)\right]$$
$$+ \frac{\partial}{\partial y}\left(\lambda\nabla\cdot\mathbf{V} + 2\mu\frac{\partial\nu}{\partial y}\right) + \frac{\partial}{\partial z}\left[\mu\left(\frac{\partial w}{\partial y} + \frac{\partial v}{\partial z}\right)\right] + \rho f_y \tag{2.19}$$

$$\frac{\partial(\rho w)}{\partial t} + \frac{\partial(\rho uw)}{\partial x} + \frac{\partial(\rho vw)}{\partial y} + \frac{\partial\left(\rho w^2\right)}{\partial z} = -\frac{\partial p}{\partial z} + \frac{\partial}{\partial x}\left[\mu\left(\frac{\partial u}{\partial z} + \frac{\partial w}{\partial x}\right)\right]$$
$$+ \frac{\partial}{\partial y}\left[\mu\left(\frac{\partial w}{\partial y} + \frac{\partial v}{\partial z}\right)\right] + \frac{\partial}{\partial z}\left(\lambda\nabla\cdot\mathbf{V} + 2\mu\frac{\partial w}{\partial z}\right) + \rho f_z \tag{2.20}$$

2.6.1.2   Energy conservation

To derive the energy equation, once more, the flow model of an extremely small fluid element in motion is utilized, as illustrated on the right side of Figure 17. The fundamental principle mentioned earlier is essentially a manifestation of the first law of thermodynamics (ANDERSON, 2011). When this principle is applied to the flow model of a fluid element moving with the flow, it asserts that The rate of change of energy within the system is equal to the sum of the heat added and the work done on the system by external actions(ÇENGEL; GHAJAR, 2020).

$$de = \partial q + \partial w \tag{2.21}$$

The volumetric heating rate, accounting for the viscous component of the equation, is defined as shown on eq 2.22.

$$\iiint_V \dot{q}\rho dV + \dot{Q}_{Viscoso} \tag{2.22}$$

Furthermore, the rate of work done is determined by multiplying velocity U by the force in the direction of velocity V. Applying this concept, it's evident that the total rate of work done on the fluid within V is equal to the scalar product of the velocity vector V with field forces, surface forces, and viscous forces, as previously performed in the derivation of momentum.

$$\mathbf{U}\left[\iiint_v \rho\mathbf{f}dV - \iint_S p\mathbf{dS} + \mathbf{F}_{Viscoso}\right] = -\iint_S p\mathbf{U}\cdot\mathbf{dS} + \iiint_V \rho(\mathbf{f}\cdot\mathbf{U})dV + \dot{W}_{Viscoso} \tag{2.23}$$

The component energy partial derivative in the First Law of Thermodynamics equation represents the total energy of the system and consists of the sum of internal energy e plus the portion of kinetic energy $(u^2)/2$. Summing the total energy of the mass flow across surface S with the change in energy within volume V yields:

$$\frac{\partial}{\partial t} \iiint_V \rho \left(e + \frac{u^2}{2}\right) dV + \iint_S (\rho \mathbf{U} \cdot \mathbf{dS}) \left(\frac{v^2}{2}\right) \tag{2.24}$$

Now using the first law of thermodynamics shown on eq 2.21 and substituting eq 2.24:

$$\iiint_V \dot{q}\rho dV + \dot{Q}_{Vis\,coso} - \iint_S \rho U dS + \iiint_V \rho(f \cdot U) dV +$$
$$\dot{W}_{Viscoso} = \frac{\partial}{\partial t} \iiint_V \rho \left(e + \frac{u^2}{2}\right) dV + + \iint_S \rho U \cdot dS \left(e + \frac{u^2}{2}\right) \tag{2.25}$$

$$\dot{Q}'_{Viscoso} = k_t T \left(\nabla \cdot \nabla^T\right)$$
$$\dot{W}'_{Viscoso} = (\nabla \cdot \tau) \cdot \mathbf{U} \tag{2.26}$$

In a similar process to the other derivations, the divergence theorem is used to transform surface integrals into volume integrals and then equal to zero. This is done with the substitution of equations 2.26, which refer to the heat transfer along the surface and work flux done by the fluid due to viscous stresses, respectively.

$$\frac{\partial}{\partial t}\left[\rho\left(e + \frac{u^2}{2}\right)\right] + \nabla \cdot \left[\rho\left(e + \frac{u^2}{2}\right)\mathbf{U}\right] = \rho\dot{q} - \nabla \cdot (p\mathbf{U}) + \rho(\mathbf{f} \cdot \mathbf{U}) + k_t T\left(\nabla \cdot \nabla^T\right) + (\nabla \cdot \tau) \cdot \mathbf{U} \tag{2.27}$$

2.6.2 Turbulence Model

Various turbulence models are available, each demanding different levels of computational resources. These models tend to perform better in specific scenarios, making the selection of a turbulence model a critical aspect for obtaining accurate results. Some models may trade precision for computational efficiency, while others attempt to strike a balance between these factors. Additionally, certain models tend to extrapolate results in particular cases, such as near-wall velocity, viscosity, and other parameters.

Given the limited computational power available for the execution of the current work, preference was given to models that provide accurate results while offering a strong representation of near-wall characteristics. That way, the simulation parameters and behaviors were essential to select the preferred turbulence method.

In the current work, both fluids and solids are involved. The fluid within the combustion chamber is accelerated to supersonic speeds and is treated as an incompressible, ideal gas, pre-mixed product. Meanwhile, for the cooling stream of water, the roughness of the wall had to be considered since the engine is 3D printed. Considering that most contemporary turbulence models are based on the Reynolds-Averaged Navier-Stokes (RANS) working principle, models such as $\kappa - \epsilon$ and ω were assessed, along with associated studies.

As described by Wilcox e Wilcox (2006), the $\kappa - \epsilon$ model consists of two coupled transport equations, one for turbulent kinetic energy (κ) and another for turbulent dissipation ϵ. On the other hand, the $\kappa - \omega$ model (WILCOX; WILCOX, 2006; SPALDING, 1991) encompasses turbulent kinetic energy κ associated with Specific dissipation rate ω.

The $\kappa - \epsilon$ model exhibits limitations when handling complex flows characterized by severe pressure gradients, separations, and strong streamline curvatures. Its most significant weakness is its insensitivity to adverse pressure gradients. Another drawback is the numerical stiffness encountered when integrating equations within the viscous sublayer, which are treated with damping functions with stability concerns (MENTER, 1992).

In contrast, the $\kappa - \omega$ model performs considerably better under adverse pressure gradient conditions and demonstrates superior performance in various scenarios, including wall-bounded boundary layers, free shear flows, and low Reynolds number flow. This makes it well-suited for complex boundary layer flows under adverse pressure gradients and separation, such as in the present case. However, it is worth noting that the $\kappa - \omega$ model may tend to predict separation as excessive and occurring earlier than observed, often requiring a high mesh resolution near the wall.

Based on previous works, (MENTER, 1992) developed the SST (Shear-Stress Transport) turbulence model, which incorporates characteristics of both the $\kappa - \varepsilon$ and $\kappa - \omega$ models. The figure represents the method transition zone near walls.

Building upon previous research, Menter (1992) introduced the SST (Shear-Stress Transport) turbulence model, which combines features from both the $\kappa - \varepsilon$ and $\kappa - \omega$ models. Figure 18 illustrates the method's transition zone near walls.
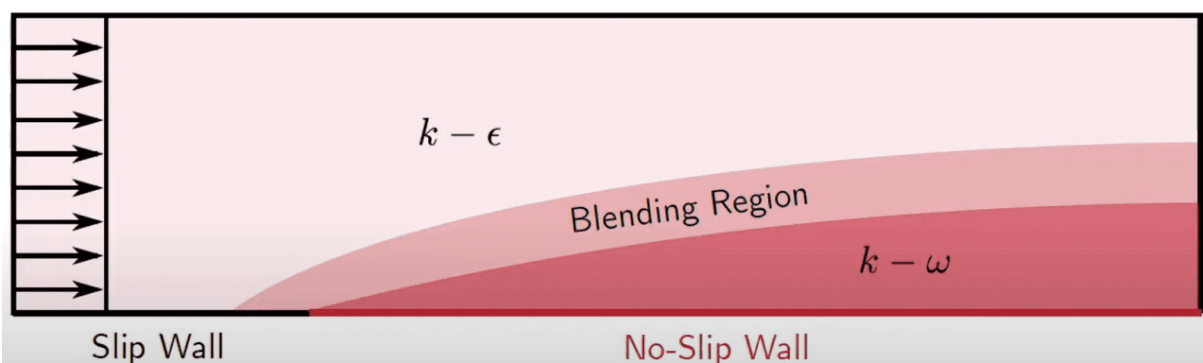
Figura 18 – The $\kappa - \omega$ SST model transitions between the $\kappa - \varepsilon$ and $\kappa - \omega$ turbulence models using a blending function. (MENTER, 1992)

As explained in his work, (MENTER, 1992) chooses the $\kappa - \omega$ model within the boundary layer, as it allows for simple boundary conditions - Dirichlet conditions - providing the model with greater numerical stability. Moving away from the boundary layer, the use of the $\kappa - \varepsilon$ model becomes more suitable since, unlike the $\kappa - \omega$ model, it is not

highly sensitive to conditions imposed in the free stream (MENTER, 1992). The transport equations describing the model are:

$$\rho \left(\frac{\partial k}{\partial t} + u_i \frac{\partial k}{\partial x_i} \right) = P_k - \beta' k \omega \rho + \frac{\partial}{\partial x_i} \left[\left(\mu + \frac{\mu_t}{\sigma_k} \right) \frac{\partial k}{\partial x_i} \right] \tag{2.28}$$

$$\rho \left(\frac{\partial \omega}{\partial t} + u_i \frac{\partial \omega}{\partial x_i} \right) = \alpha \rho S^2 + \beta \rho \omega + \frac{\partial}{\partial x_i} \left[\left(\mu + \frac{\mu_t}{\sigma_\omega} \right) \frac{\partial \omega}{\partial x_i} \right] + 2 \left(1 - F_1 \right) \rho \sigma_{\omega 2} + \frac{1}{\omega} \frac{\partial k}{\partial x_i} \frac{\partial \omega}{\partial x_i} \tag{2.29}$$

Given that ε is the turbulent dissipation, ω is the turbulent frequency, β, β', σ_k, σ_ω, and α are the empirical constants of the turbulence models (MENTER, 1992). The turbulent viscosity is defined by considering the transport of the principal turbulent shear stresses (WILCOX; WILCOX, 2006), so we have:

$$v_t = \frac{\alpha_1 k}{\max \left(\alpha_1 \omega, \left(S_{ij} S_{ij} \right)^{1/2} F_2 \right)} \tag{2.30}$$

Where $\sqrt{S_{ij} S_{ij}}$ is an invariant measure of the rate of deformation tensor.

It's worth noting that in the formulation, two blending functions, $F1$ and $F2$, were used. Both are defined based on the distance to the wall and flow variables, and their values modify the transport equations. The first blending function, $F1$, in Eq. 2.30, serves to switch between turbulence models as well as determine the model constants. It has a value of zero in the far wall region (representing the $\kappa - \varepsilon$ model) and a value of 1 in the boundary layer (representing the $\kappa - \omega$ model) (MENTER, 1992). The $F1$ function is defined as:

$$F_1 = \tanh \left(\text{arg}_1^4 \right) \tag{2.31}$$

$$\text{arg}_1 = \min \left[\max \left(\frac{\sqrt{k}}{\beta' \omega}, \frac{500 \nu}{y^2 \omega} \right), \frac{4 \rho \sigma_{\omega 2} k}{CD_{k\omega} y^2} \right] \tag{2.32}$$

$$CD_{k\omega} = \max \left(2 \rho \sigma_{\omega 2} \frac{1}{\omega} \nabla k \nabla \omega, 1, 0.10^{-10} \right) \tag{2.33}$$

The second blending function, $F2$, is responsible for switching between turbulence models in the formulation of turbulent viscosity and is given by eq 2.34, representing a transitioning function between models.

$$F_2 = \tanh \left(\text{arg}_2^2 \right) \tag{2.34}$$

$$\arg_2 = \max\left(\frac{2\sqrt{k}}{\beta'\omega y}, \frac{500\nu}{y^2\omega}\right) \tag{2.35}$$

Finally, we use a limiter to produce turbulent kinetic energy to prevent turbulence growth in stagnation regions. This limiter is given by the formula 2.36

$$P_k = \mu_t \frac{\partial u_i}{\partial x_j}\left(\frac{\partial u_i}{\partial x_j} + \frac{\partial u_j}{\partial x_i}\right) \tag{2.36}$$

Where $\tilde{P}k$ is equal to:

$$\tilde{P}_k = \max\left(P_k, 10 \cdot \rho\beta^* k\omega\right) \tag{2.37}$$

In addition, the $\kappa-\omega$ SST model will be used in *Ansys Fluent*, where other relevant parameters, such as wall roughness, can be defined for this specific model.

3 Methodology

Typical CFD software uses a 3-step workflow: preprocessing, solution, and post-processing. Preprocessing entails configuring a fluid flow problem within a CFD software program; in this case, ANSYS was employed. This stage encompasses defining the geometry of the region of interest (computational domain), dividing this domain by creating a mesh, specifying physical and chemical properties, setting flow properties, and establishing boundary conditions for cells that correspond to the domain boundaries (VERSTEEG; MALALASEKERA, 2011).

In the finite element method, the solver resolves the problem through several steps: integrating the governing equations of fluid dynamics across all control volumes within the domain, transforming the resulting integral equations into a system of algebraic equations (discretization), and solving the problem using an iterative method (VERSTEEG; MA-LALASEKERA, 2011), as demonstrated on chapter 2.6. The numerical solution presents its results in various formats on the display after the calculations and can be interpreted in diverse ways. This process of visualizing and analyzing the results is referred to as post-processing.

3.1 Simulation geometry and boundary conditions

The domain studied in this work includes the internal region of the combustion chamber and walls, along with the respective cooling channels of the SARA v3 rocket. Considering the observed symmetry in the cylindrical-shaped body, a 1/60 section of the motor's cross-sectional area is employed to optimize computational efficiency (image 19). Figure 20 illustrates the domain and geometry developed in the *Space Claim* tool.
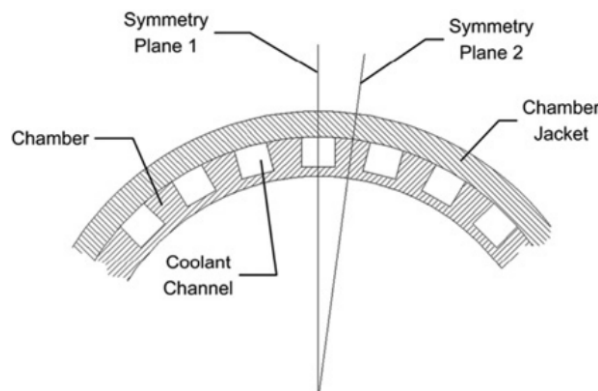

Figura 19 – Schematic view of solution domain symmetry selection (ULAS; BOYSAN, 2013)

The geometry presents only half of the channel's width along with its adjacent channel wall, as symmetry conditions on its sides characterize it. This configuration makes it easier to analyze fluid flow through the center of water channels.
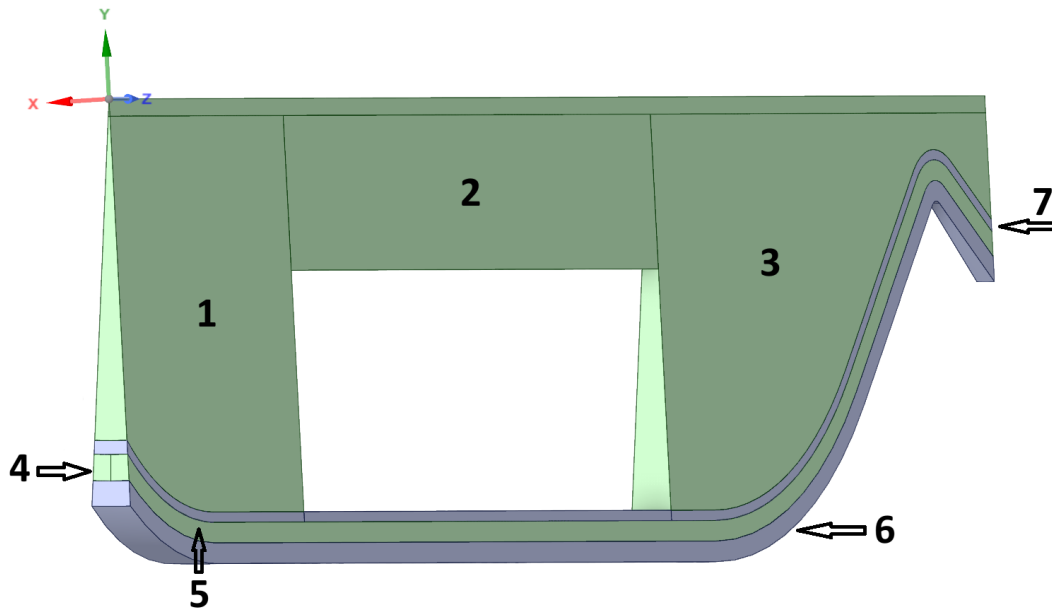

Figura 20 – Final Geometry and Domain for analysis. (Author)

Zones 1, 2, and 3 correspond to the internal section of the combustion chamber and nozzle, representing the presence of the hot pre-mixed gases considered in the simulation. These gases accelerate through the convergent-divergent nozzle at the final section of the engine. Zones 6 and 7 depict the internal and external walls, respectively, with their thicknesses and spacing determined by the geometry obtained by CPL (SHYNKA-RENKO, 2022) during the engine development.

Zone 5 defines the volume of water intended for cooling the engine. Meanwhile, Zone 4 represents the supporting wall that bridges the internal and external walls.

The simulation omits the paraffin grain, replacing it with a hole in the geometry. This decision stems from the unrealistic temperatures observed in the grain without an abrasive simulation character, involving ablation, mixing, and chemical reactions with the injected nitrous oxide in the combustion chamber. Conducting a simulation considering the mixture of the oxidizer and fuel becomes unnecessary from a thermal perspective as the properties of the premixed gas are known. Furthermore, paraffin's low thermal conductivity, being five times less conductive than Inconel 718, categorizes it as a thermal insulator, preventing heat transfer to the internal walls, thus being useless from a cooling perspective.

The simulation involves two fluids flowing through separate regions and solid walls made of Inconel 718. "combustion products"are introduced in the combustion chamber,

considering a pre-mixed mixture. These gases then flow towards the nozzle, accelerating and exiting through.

For the water coolant passage, there is a defined gap in the engine geometry and wall thickness, as determined by CPL's work, with the inlet being the nozzle and the exit being the initial portion of the combustion chamber. Figure 21 shows the visualization of both inlets and outlets. The inlet and outlet for the water are represented by letters A and B, respectively, while combustion products are represented by C and D.
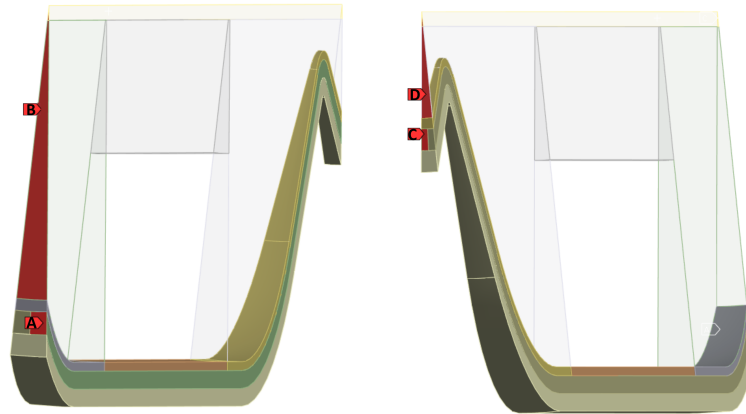

Figura 21 – Inlet and outlets of water and combustion products (Author)

The combustion products, characterized by a viscosity of 1.7894×10^{-5}, kg/(m.s) and a molecular weight of 28.966 $kg/kmol$, was the first material defined. As outlined in graph 22, the ideal gas model determines density, thermal conductivity, and specific heat. The mass flow inlet configuration for the combustion products was set with an initial temperature of 1710 K, at 0,0067 kg/s, and an initial supersonic gauge pressure of 3378432 Pa. Turbulence parameters included an intensity of 5% and a turbulent viscosity ratio of 10. The exhaust port was configured as a pressure outlet with a gauge pressure of 1 atm at reverse flow prevention configuration. Pre-mixed combustion chamber parameters were dedicated to temperature profiles and data from previous works done in the CPL lab, including the last Cientific initiation project done by the author.

For the solid region, Inconel 718 was employed. It is a high-strength, heat-resistant metal suitable for advanced applications and can be utilized in a metal 3D printer. Inconel 718 has a density of 8440 kg/m^3, while its thermal conductivity and specific heat (see Figure 23) are correlated with the material temperature.

The water inlet was configured with a mass flow of 0.0064 kg/s at 300K, with a turbulent intensity of 5%, followed by a turbulent viscosity ratio of 10, for the first simulation, done for grid convergence purposes. In addition, the water outlet was set as a pressure outlet with the external pressure equal to 1 atm. All water properties defined are constant due to the slight variation with temperature change, as shown in Table 1 below:
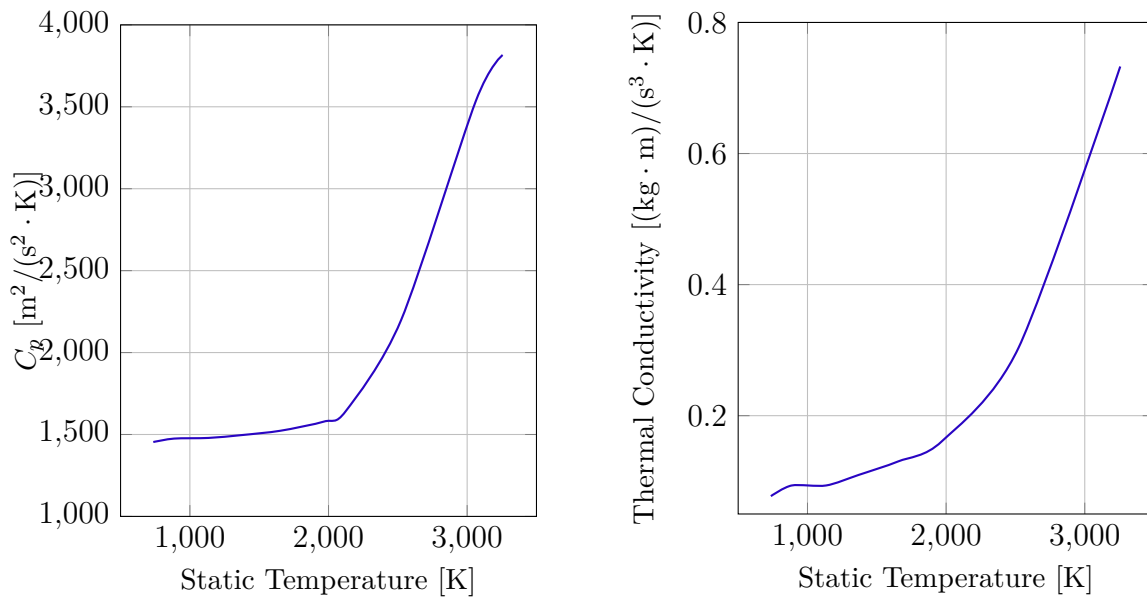
Figura 22 – (Left) Specific Heat Capacity vs Static Temperature. (Right) Thermal Conductivity vs Static Temperature for "combustion products. (Author).
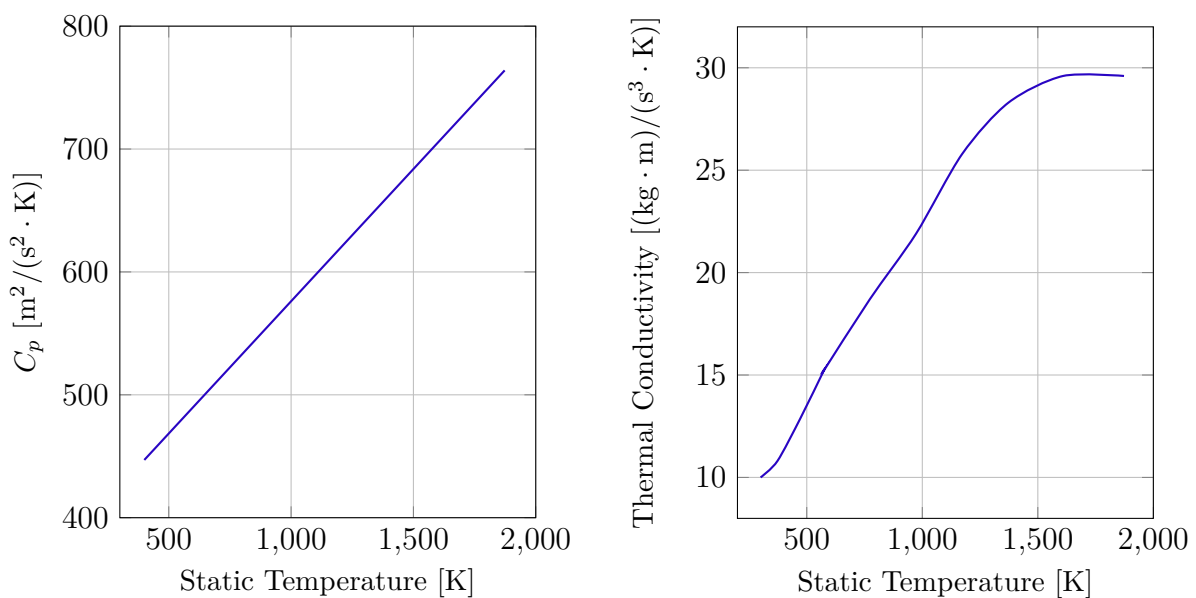

Figura 23 – (Left) Specific Heat Capacity vs Static Temperature. (Right) Thermal Conductivity vs Static Temperature for Inconel (Author).

Tabela 1 – Water constants used for simulation (KESTIN et al., 1984)

|	
ρ @ 300 K	998 kg/m^3
Viscosity	0.758 kg/(m.s)
Thermal conductivity	0.6 $W/m.K$
Specific Heat	4182 $J/kg.K$

A sand grain roughness model was employed to enhance the roughness representation resulting from the additive manufacturing process. The model included a maximum roughness height of 1mm and a constant of 0.5. This constant essentially governs the periodicity between the minimum and maximum height of the rough wall.

Two parameters will be evaluated to analyze the performance of different channel arrangements: the overall number of channels and each channel's width (and consequently the aspect ratio). This selection is based on previous works by the author (ULAS; BOYSAN, 2013), demonstrating the presence of an optimal characteristic using the same methodology.

A total of 5 different channel widths was chosen, and later, the comparison between different numbers of tubes was also added, where tables 7 and 9 show five different configurations selected for simulation. The subsequent tables below show the selected geometries of both water channel widths and the total number of channels, configuring ten simulations.

Since the distance between chamber walls is fixed by design, to increase or decrease the number of channels while maintaining a set aspect ratio, the thickness of each support wall (between channels) is altered accordingly. The minimum possible thickness is defined by the printing limitations of the selected printer, usually on a millimeter scale (FRAZIER, 2014).

Tabela 2 – Parameters for channel width configuration (Author)

	3 x 6 x n	3 x 5 x n	3 x 4 x n	3 x 3 x n	3 x 2 x n
Channel height [mm]	3	3	3	3	3
Channel width [mm]	6	5	4	3	2
number of cooling channels	30	30	30	30	30
AR (aspect ratio)	0.5	0.6	0.75	1	1.5
$\dot{m}$ (per channel) [kg/s]	0.0124	0.0124	0.0124	0.0124	0.0124
Channel geometry					

The letter "n"on Table 7 represents the channel width in millimeters, while the letter "m"on 9.

Tabela 3 – Parameters for number of channel configuration (Author)

	3 x m x 15	3 x m x 30	3 x m x 45	3 x m x60	4 x m x 75
Channel height [mm]	3	3	3	3	3
Channel width [mm]	2	2	2	2	2
number of cooling channels	15	30	45	60	75
$\dot{m}$ (per channel) [kg/s]	0.0246	0.0123	0.0082	0.0062	0.0049

3.2   Mesh

With the geometry set, the mesh was developed. The computational domain discretization procedure typically employs two techniques: structured and unstructured meshes (ANSYS, 2011). According to (SOUSA, 2005), structured meshes maintain an indexing structure in the subdivision of the domain, simplifying the identification of elements based on their indices. A structured approach also provides higher accuracy and lower numerical errors as it fits well to boundary conditions and has smooth transitions between elements. However, structured meshes have limitations, such as difficulty handling complex geometries, curved boundaries, or irregular regions.

On the other hand, unstructured meshes do not preserve this aspect, and identification is performed through neighborhood relationships, making them suitable for more complex geometries where implementing a structured mesh is challenging (SOUSA, 2005). Therefore, given the simplicity of the rocket engine's geometry, a structured mesh was developed, with all elements being quadrilaterals.

The parameter y^+, comparable to the local Reynolds number, is a non-dimensional measure in Computational Fluid Dynamics (CFD) to assess the mesh refinement for a given flow. It signifies the ratio of turbulent to laminar influences within a cell. Near the wall, viscous damping reduces tangential velocity fluctuations, while kinematic blocking diminishes normal fluctuations. Moving towards the outer part of the near-wall region, turbulence rapidly amplifies due to the production of turbulent kinetic energy resulting from significant gradients in mean velocity (SALIM; CHEAH, 2009).

Precise representation of the flow in the near-wall region is pivotal for accurately predicting wall-bounded turbulent flows. For effective near-wall modeling, it is highly recommended to maintain $y^+ <2.5$ on the near-wall region for turbulent flows (ANSYS, 2011).

With the desired y^+, correct elent size can be determined through formula 3.1 (ANDERSON, 2010):

$$y_d = \frac{y^+ \mu}{\rho u_*} \tag{3.1}$$

Where y_d, u_*, ρ, and μ are the wall distance, friction velocity, density of the fluid,

Tabela 4 – Properties needed y_{dist} determination for water region (KESTIN et al., 1984)

Target near wall y^+	5
Dynamic viscosity (μ)	0.89 mPa.s
ρ @ 300k	998 kg/m^3
Average freestream velocity (V)	0.758 m/s
Characteristic distance (L)	119 mm

and dynamic viscosity, respectively. Also, u_* is equal to:

$$u_* = \sqrt{\frac{C_f U_f^2}{\rho}} \tag{3.2}$$

Where C_f skin friction coefficient and U_f free stream velocity. There are many possible approximations to C_f, all based on Reynalds number, therefore more C_f, according to (SALIM; CHEAH, 2009) we have:

$$C_f = 0.074 Re_x^{0.2} \tag{3.3}$$

With Reynolds number:

$$C_f = \frac{0.074 \rho V L^{0.2}}{\mu} \tag{3.4}$$

$$L = \frac{4A}{O} = \frac{4 \cdot \text{ cross section of fluid in the channel}}{\text{perimiter in contact with fluid}} \tag{3.5}$$

Where V is the known freestream velocity, and L is the characteristic distance of the body. In this case, the body can be considered a squared channel, and the characteristic distance can be approximated according to Equation 3.5 (ANDERSON, 2011), yielding a characteristic distance of approximately 119 mm. All additional data used for calculating the final element size y_d is provided in Table 4.

Calculation using formulas 3.1 and 3.1 with inputs found in table 4 results in a near wall element size off $3.64.10^{-6}$ m. This is used as an initial guess for mesh refinement presented in figure 24.

The domain had to be subdivided to appropriately size and distribute elements correctly, as seen in Figure 20. This allowed the creation of element sizing elements that subdivided the lines of the geometry into a defined number of elements, resulting in the preliminary mesh seen in Figure 24, along with a focused view of the nozzle in Figure 25.

In addition to determining the correct number of divisions for each element sizing, a bias is employed to place more elements near walls with fluid contact. This refined mesh near walls facilitates the visualization of boundary layer effects on the chamber and
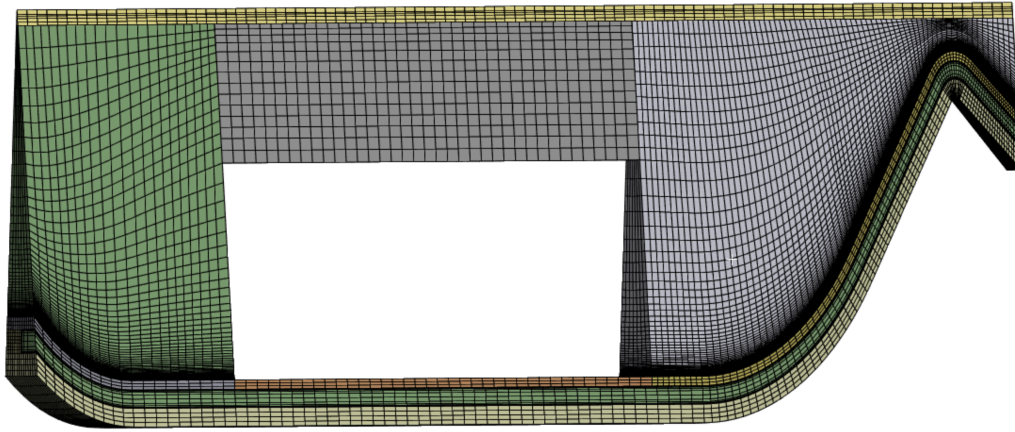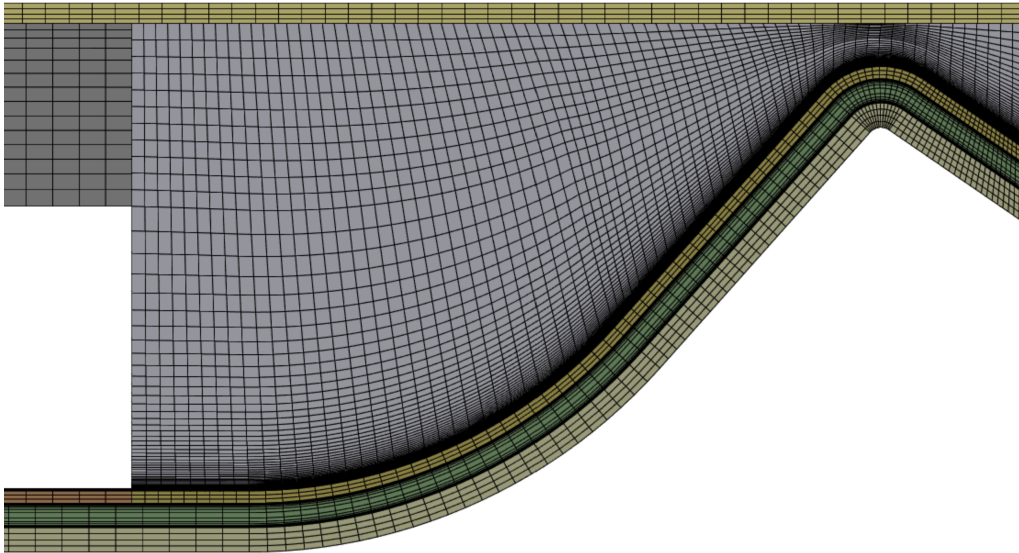
Figura 24 – Preliminary mesh (Author)

Figura 25 – mesh at nozzle and proximity (Author)

water channel, as seen in Figures 26 and 27. The combustion products zone, denoted by the number 4 in Figure 26, exhibits element refinement near walls, as does region 2, representing the water channels. It's also worth noting that regions 1 and 3, representing the solid walls, have a homogeneous mesh.
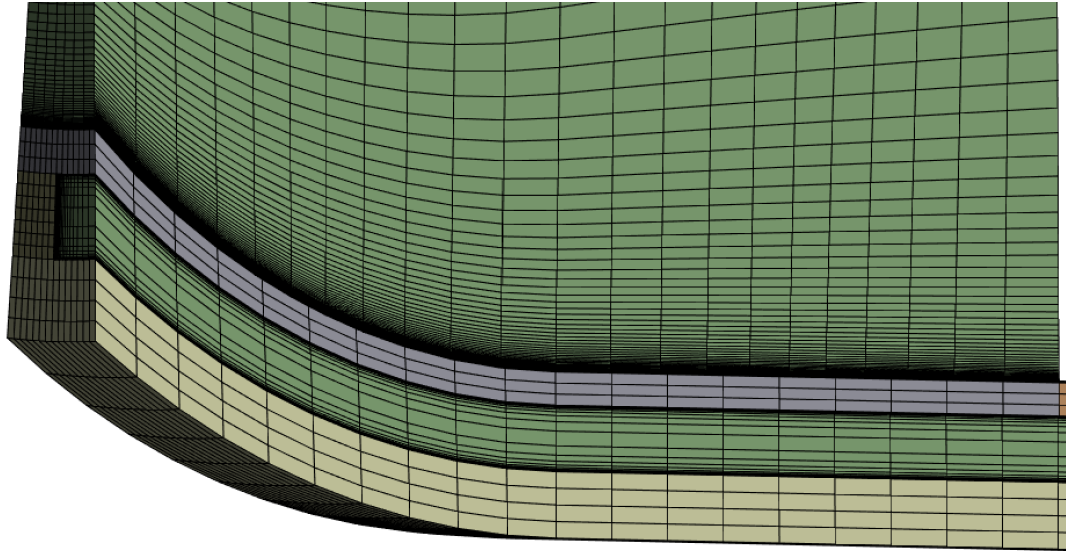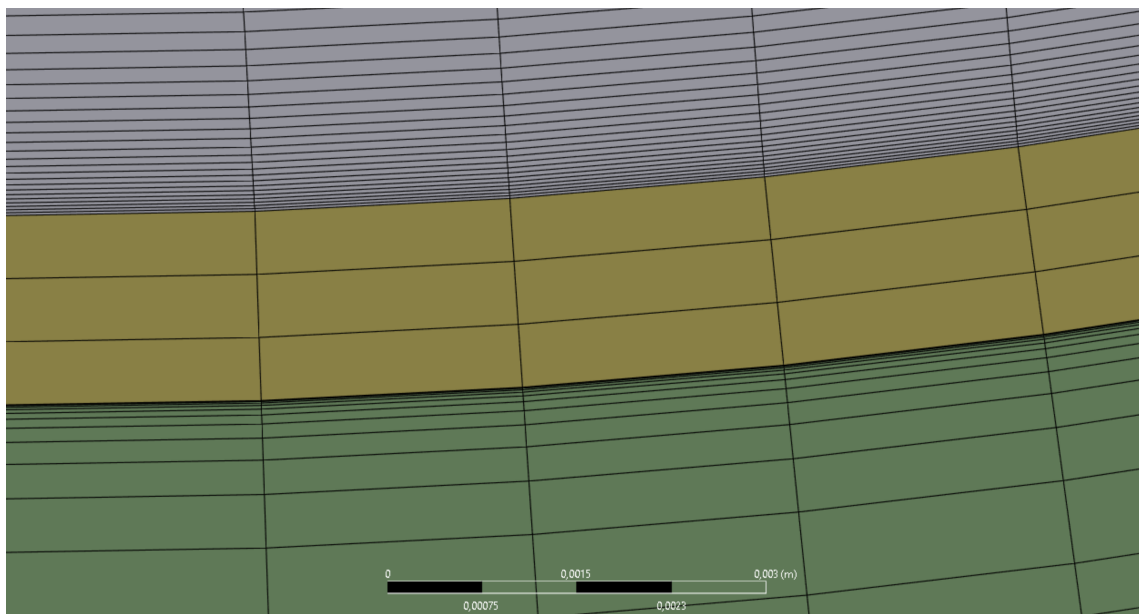
Figura 26 – Zones of the mesh (Author)

Figura 27 – Mesh refinement near walls (Author)

The mesh must be appropriately refined for a correct velocity profile and shear distribution near walls. There are several strategies for determining an accurate mesh; however, many necessitate extensive mesh testing and consume time (SALIM; CHEAH, 2009). For the present work, a grid convergence setup was selected.

3.2.1 Grid convergence

The computational domain is divided into five distinct regions: the inner and outer walls, the coolant region, the combustion chamber, and the support walls. The coolant domain is discretized using five mesh densities, focusing on near-wall regions.

This refinement aims to accurately capture the water boundary layer flow and enhance the overall precision of the results.

Hexahedral elements are employed for both the solid and coolant regions. Table 5 presents a detailed overview of the grid specifications for each of the five cases, Figure 28 illustrates a cross-sectional view of the computational domains analyzed, starting with less refined, below 25μm to most refined at 2μm.

Tabela 5 – Grid specifications for the five evaluated cases (Author)

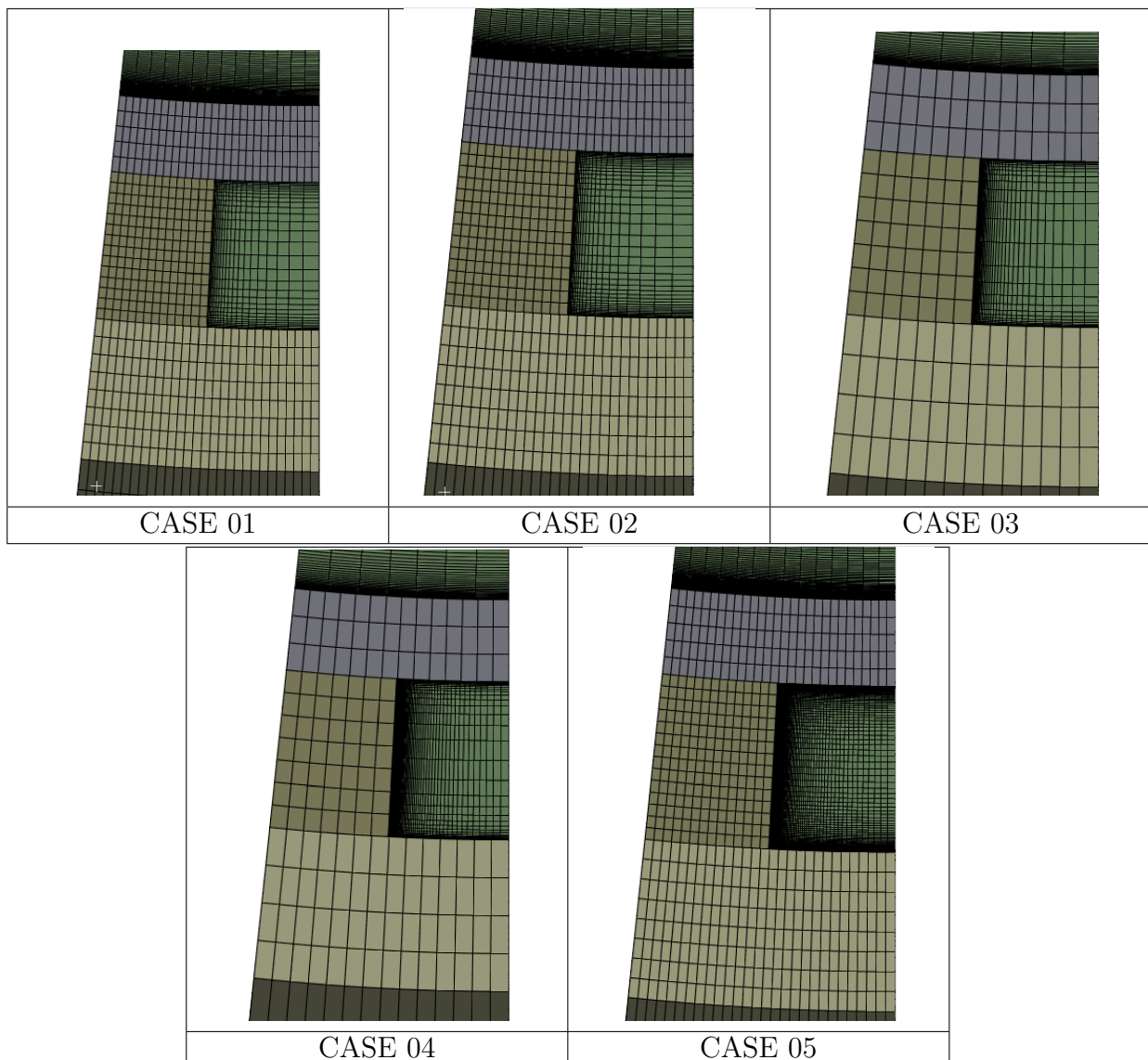|	Case 1	Case 2	Case 3	Case 4	Case 5
Wall Elements	21378	21378	21378	21378	21378
Coolant Elements	61906	145346	242643	300000	2405378
Max Element Thickness (coolant)	25 μm	20μm	10μm	5μm	2μm
Min element Thickness (coolant)	4,5 μm	3,5μm	2μm	1μm	0,2μm

Figura 28 – Cooling System Configurations (Author)

All five simulations used a pressure-based solver with a second-order discretization scheme, adhering to the boundary conditions specified in the dedicated section. The combustion chamber mesh refinement was deliberately excluded from this grid independence study, as it was adopted from previous work completed as part of a scientific initiation program done at CPL.

The simulations employed a pseudo-transient approach and typically required approximately 8000 iterations to achieve satisfactory convergence of the results. Across all five cases, the residual reports exhibited remarkable similarity, indicating consistent convergence behavior. A representative residual plot for one of the cases is provided below (Figure 29), with case 3 as an example.

Due to the inherently turbulent flow within the combustion chamber, particularly in the aft and pre-grain recirculation zones, the residuals exhibit persistent fluctuations even after achieving convergence criteria, visible starting around 5 thousand iterations up to the end of the simulation.
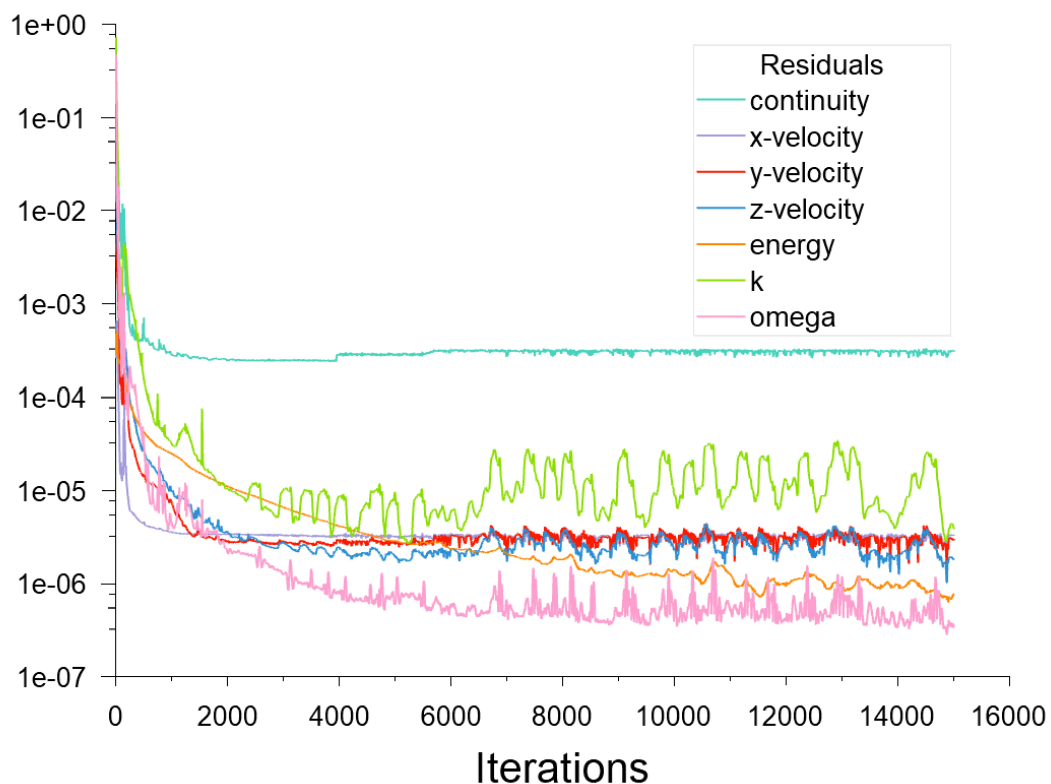

Figura 29 – Residual plot for Case 3 (representative of all cases). (Author)

Case 4 emerges as the optimal choice for mesh refinement, balancing accuracy and computational cost. Results, particularly for Temperatures, decrease by [Percentage decrease only by about 0.5%, indicating convergence in Case 4. Critical variables like water pressure show minimal variation between Cases 3 and 4. While finer meshes (e.g.,

Tabela 6 – Grid results for the five evaluated cases (Author)

	Case 1	Case 2	Case 3	Case 4	Case 5
Max Inner wall temp (K)	969.57	967.29	966.05	965	965
Max water temp (K)	705.6	701.1	698	696.6	695.8
Max yplus	3.6	2.8	1.7	0.75	0.66
Pressure drop (bar)	0,098 bar	0,096 bar	0,096 bar	0,096 bar	0,096 bar
Coolant Elements	61906	145346	242643	300000	2405378
Max Thickness (coolant)	25 μm	20μm	10μm	5μm	2μm
Min Thickness (coolant)	4,5 μm	3,5μm	2μm	1μm	0,2μm

Case 5) might offer slight improvements, the increased computational cost might not be justified given the substantial gains in Case 4. In addition, the minimum plus values for the case fall below the desired threshold of 2.5, as seen in the literature, staying at only 0.75 maximum.

Figure 30 confirms Case 4's convergence for water temperature, with minimal difference observed between Cases 4 and 5. This suggests finer refinements are unnecessary. Moreover, the 5μm refinement aligns with the initial analytical element size guess, further supporting convergence on an appropriate mesh.
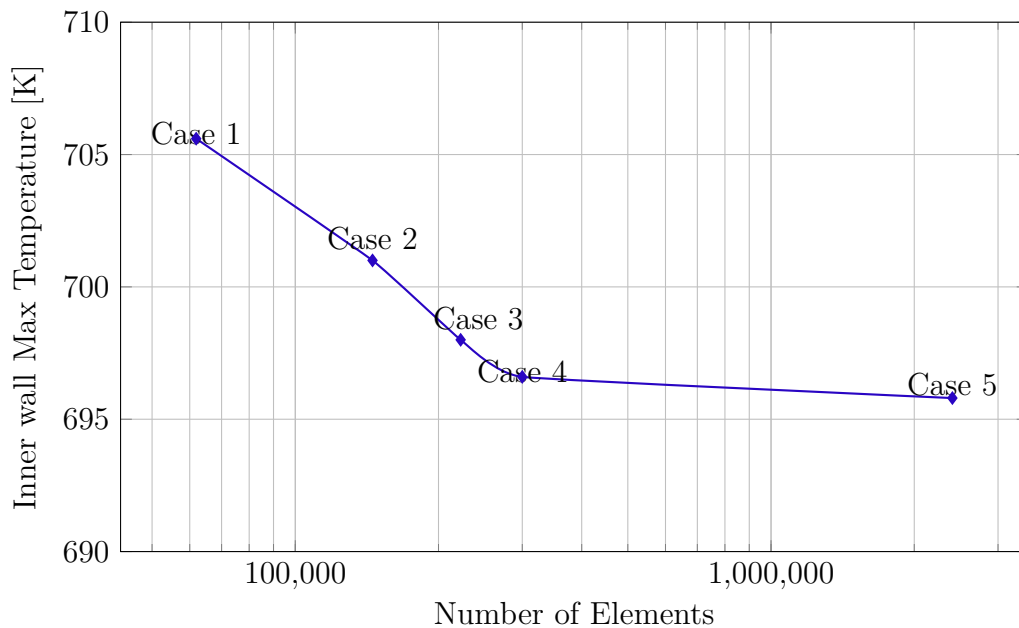

Figura 30 – Inner wall Max Temperature vs Number of Elements

In addition to the grid convergence, mesh metrics can be used further to evaluate the mesh quality of the selected refinement. According to the Ansys Manual (ANSYS, 2011), orthogonality values between 0.15 and 0.2 are considered acceptable, while values above 0.7 are regarded as very good to excellent, with 1 being the ideal; this is visible on graph 31.
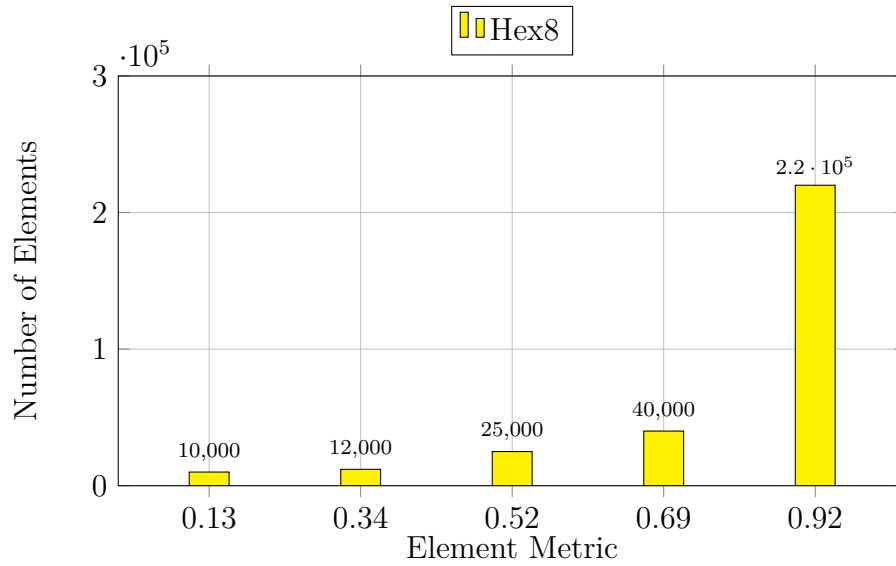
Figura 31 – Bar chart representing the number of elements against the orthogonality.

Mesh quality, as measured by skewness, is satisfactory. Acceptable values range from 0.8 to 0.94, with values below 0.5 considered excellent (zero being ideal) (ANSYS, 2011). Figure 32 confirms that the element skewness values fall within the acceptable range, ensuring a suitable mesh for our analysis.
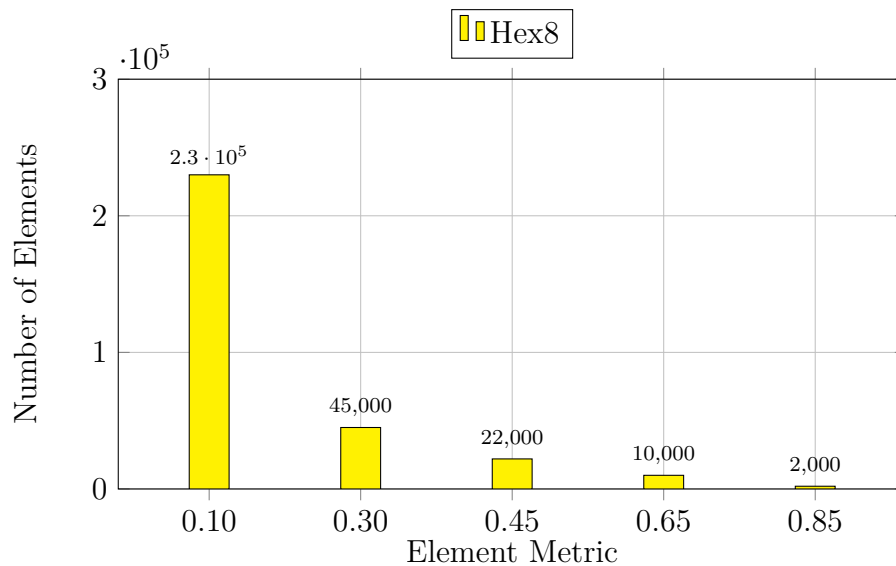

Figura 32 – Bar chart representing the number of elements against the orthogonality.

3.3   Final Setup

The following considerations and definitions were used for solution setup:

- Pressure-based solution

- Pseudo-transient solution, with approximately 8,000 iterations of proper convergence (10,000 total iterations).

- Energy equation with textitk-ω SST turbulence model

- Implicit formulation with second-order upwind flow simulation

- Second-order spatial discretization method for turbulent kinetic energy and specific dissipation rate.

- Water mesh refinement of 5μm

- Sand grain model was used to model rough surfaces on 3D printed surfaces. The model used the default parameters set by Ansys.

The set of images 33 and 34 represent geometries used for the channel aspect ratio and total number of channels simulations. Image 33 presents the geometries employed to define channel aspect ratios, ranging from 2 mm to 6 mm, totaling 5 cases. Meanwhile, image 34 showcases the geometries used for the number of channel cases.

While a standard of 30 channels with a fixed mass flow rate corresponding to the motor's sectional area is used for water channel sizing simulations, the number of channel cases deviates from this approach. Here, the sectional area and the corresponding mass flow condition are adjusted for each case. This ensures that the overall motor condition of 0.37 kg/s oxidant inlet remains consistent.
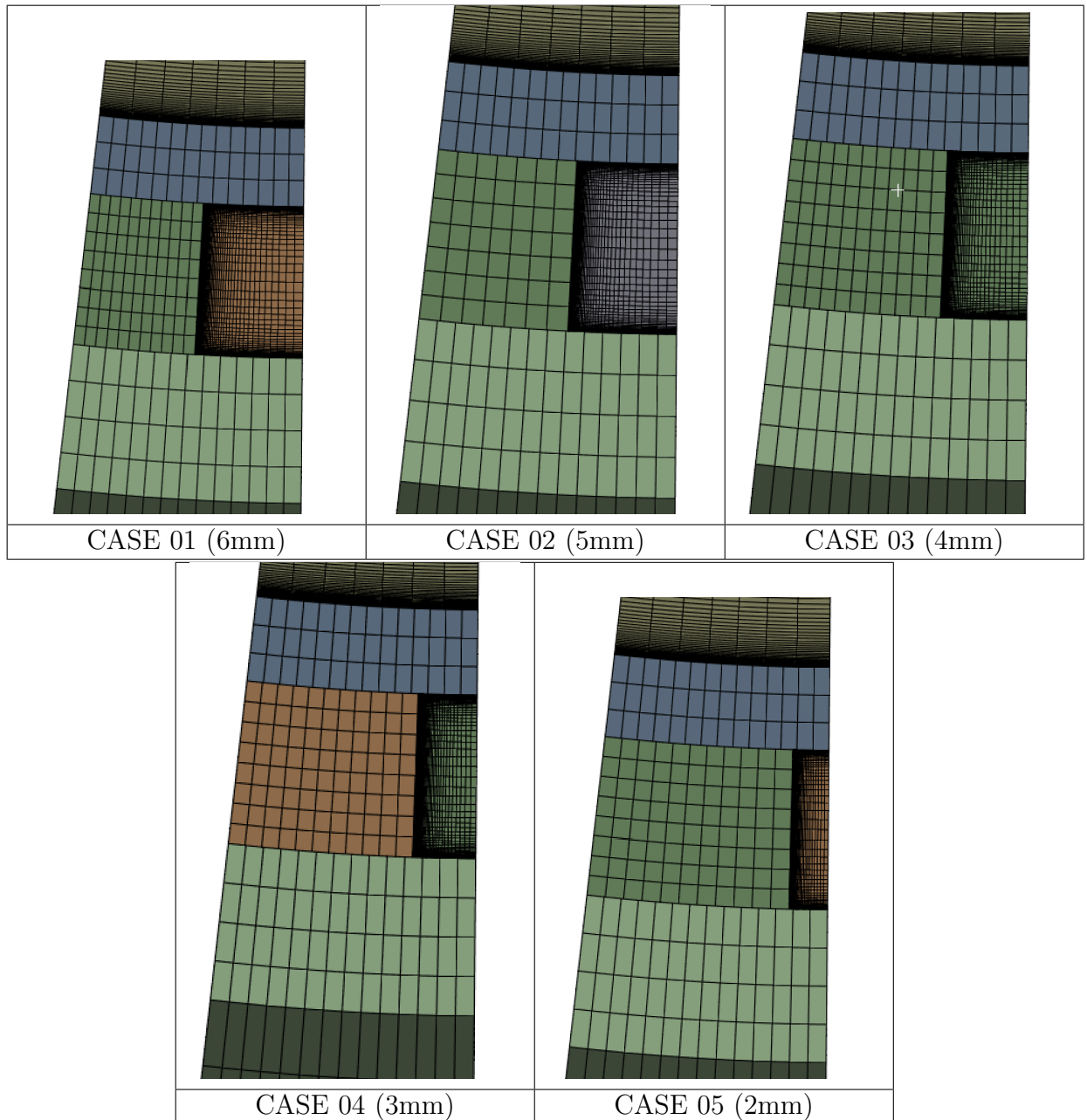
Figura 33 – Cooling System Configurations regarding channel width configuration (Author)
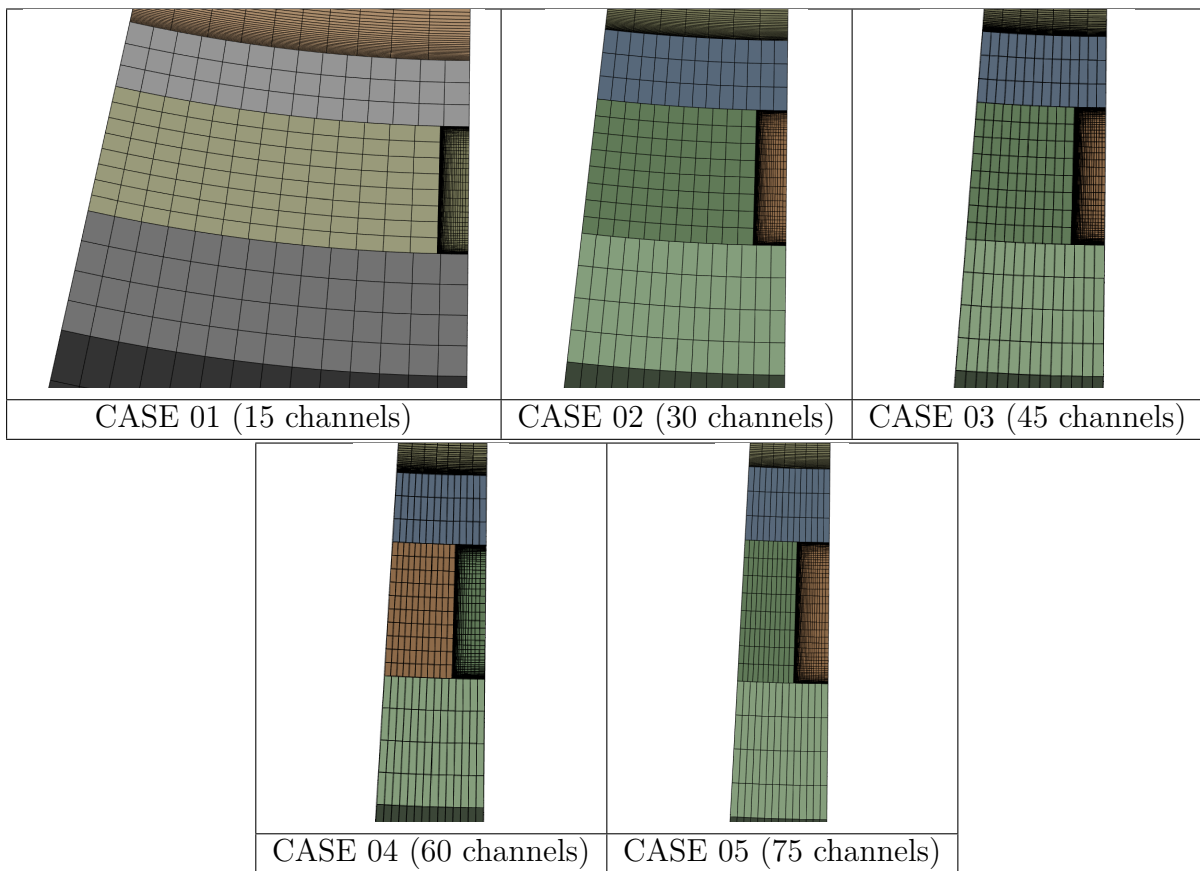
Figura 34 – Cooling System Configurations regarding total number of channels(Author)

4 Results

This chapter explores a two-step approach to identifying the optimal water channel design. As discussed previously, the first step investigates the influence of five water channel geometries on system performance.

The second step utilizes the findings from the first step to analyze the impact of the number of channels using the optimal channel thickness identified earlier. This analysis aims to determine the optimal channel width and number combination for further in-depth investigation.

4.1 Results for the water channels thickness

All five simulations utilized identical setups to ensure a fair comparison: boundary conditions, model configurations, and 10,000 iterations remained constant. Each simulation began with an initial temperature of 300 K and a velocity of 7 m/s. The results reveal an interesting trend: performance, measured by maximum inner wall temperature, improves as channel size increases, as seen in table 7. This is likely due to increased flow area and potentially more efficient heat transfer with larger channels. Additionally, lower average and maximum water temperatures observed with larger channels support this notion of improved heat dissipation.

Tabela 7 – Parameters for channel width configuration (Author)

	3 x 6 x 30	3 x 5 x 30	3 x 4 x 30	3 x 3 x 30	3 x 2 x 30
Channel height [mm]	3	3	3	3	3
Channel width [mm]	6	5	4	3	2
number of cooling channels	30	30	30	30	30
AR (aspect ratio)	0.5	0.6	0.75	1	1.5
$\dot{m}$ (per channel) [kg/s]	0.0124	0.0124	0.0124	0.0124	0.0124
Channel geometry					

Table 7 depicts the actual geometries that only half are simulated due to applying a symmetry condition. This efficient approach significantly reduces simulation time and resources. Importantly, the symmetry condition still allows for a clear visualization of the water's boundary layer and internal flow profile within the channel, providing valuable insights into the system's behavior.

Figures 35 and 36 elucidate the characteristic pressure and velocity profiles within the standardized combustion chamber model employed throughout this study. Figure 35

reveals the expected pressure decrease in the throat region, corresponding to the expansion and acceleration of the combustion gases. This acceleration is further evident in Figure 36, which demonstrates the attainment of sonic flow (Mach 1) at the throat, followed by a transition to supersonic velocities in the diverging nozzle section.
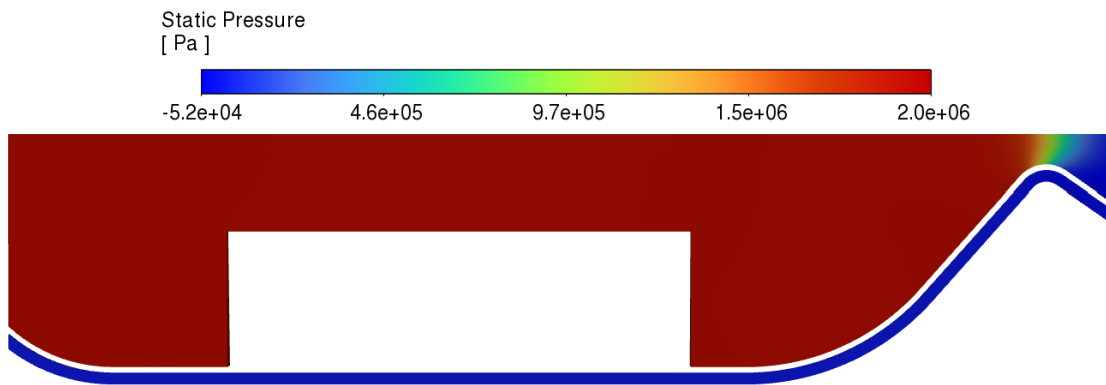
Figura 35 – Chamber static pressure (Author)
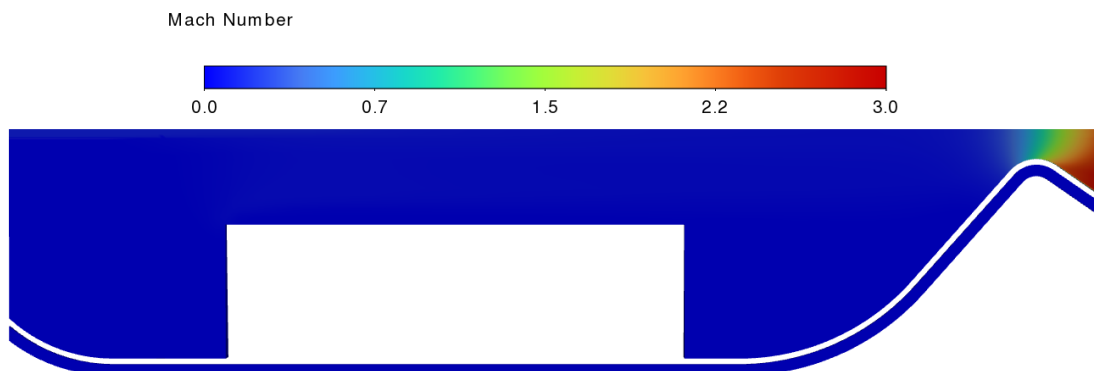
Figura 36 – Mach number at the chamber (Author)

The temperature distribution within the combustion chamber for the 2mm case is illustrated in Figure 37. Inlet gases enter at 1710 K, and a subsequent temperature drop post-throat region confirms the presence of a converging-diverging nozzle. Notably, recirculation zones upstream and downstream of the grain exhibit lower temperatures, highlighted by yellow shading in the figure. While wall profiles vary between simulations, the overall chamber conditions remain consistent.

Figura 37 – Static temperature in the chamber (Author)

Table 8, the most pertinent data for each simulation are seen. The case that demonstrates the best overall performance is the thinnest channel, at 2mm.

Tabela 8 – Simulations done for difference water channel widths and subsequent data

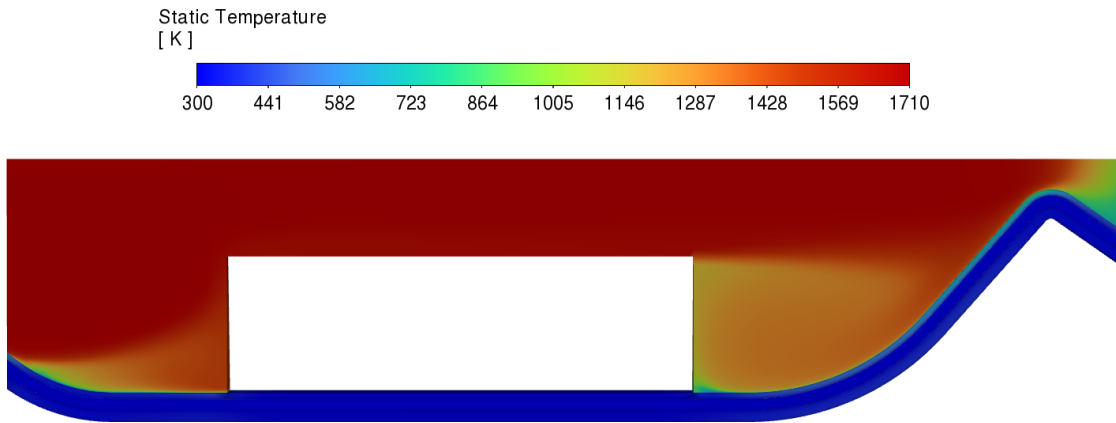| Maximum water channel width [mm]	6	5	4	3	2
Max inner wall temperature [K]	942	934.4	924	914	904.1
Pressure drop [bar]	0,097	0,122	0,199	0,4	1,23
Max water temperature [K]	674	656.3	627.5	596	554.4
Average water temperature [K]	308.7	308.5	308.3	307.9	307.3
Average water velocity [m/s]	0.78	0.87	1.07	1.40	3.66
Flow max velocity [m/s]	4.3	5.68	7.1	9.5	15.8
Total number of channels	30	30	30	30	30
Aspect ratio	0.5	0.6	0.75	1	1.5

Also, analyzing the impact of channel high, similar to the 8mm configuration used by (ULAS; BOYSAN, 2013), could be valuable. Their work suggests diminishing returns when doubling channel height from 3mm, indicating a potential trade-off to consider. However, since the distance between walls is 3mm for the final project at the SARA V3 motor, such height modifications were not considered possible in this analysis.

While larger channels generally lead to better thermal performance, printability considerations also play a crucial role. Additive manufacturing techniques can struggle with very small channel features. Therefore, the optimal channel size necessitates a trade-off between achieving the best thermal performance and maintaining a feasible manufacturing complexity.

Current PBF 3D metal printing capabilities, particularly in Brazil, are often limited to features on the millimeter scale. Although the initial channel design might call for a 2mm throat width, achieving this region's desired 0.4mm minimum feature size presents significant manufacturing challenges.
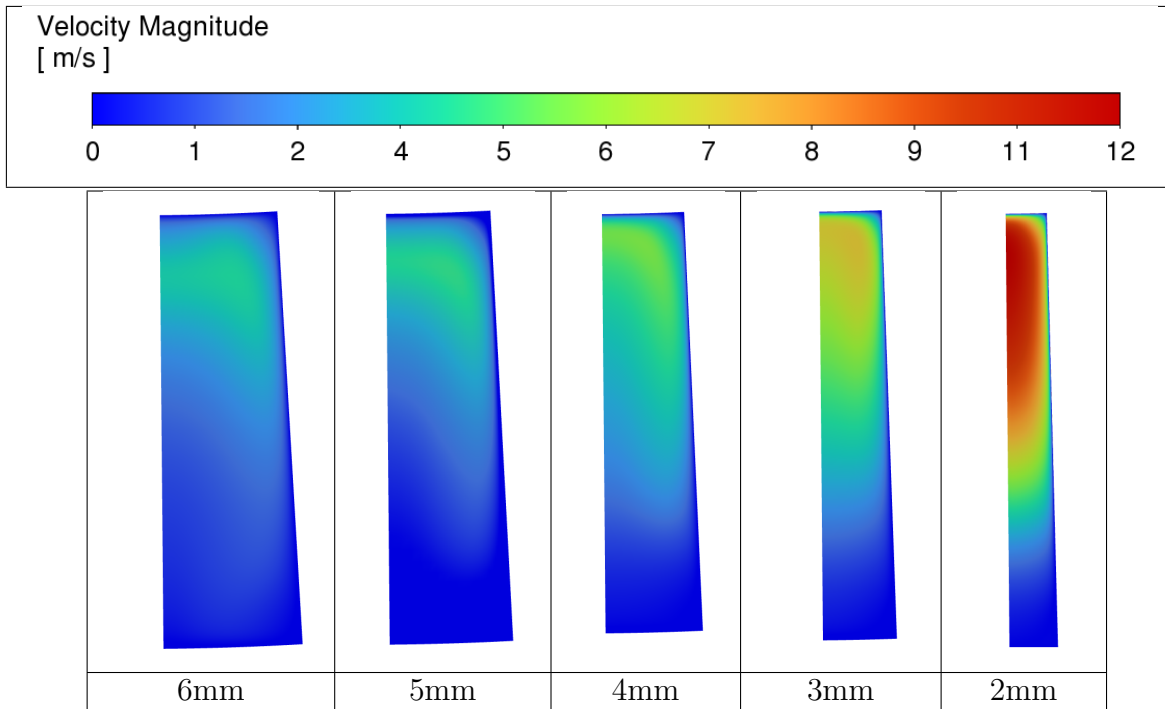
Figura 38 – Velocity profile at water outlet for different channel geometries (Author)

However, although differences between different channels are not big in modulus, they clearly show a trend: As the water channel width decreased, the velocity profile and pressure variations increased significantly. This relationship was most pronounced at the nozzle outlet and throat region (Tables 38 and 4.1), with narrower channels consistently demonstrating the highest velocities. The velocity profile differences gradually decreased with increasing channel width, as illustrated in Graph 41.
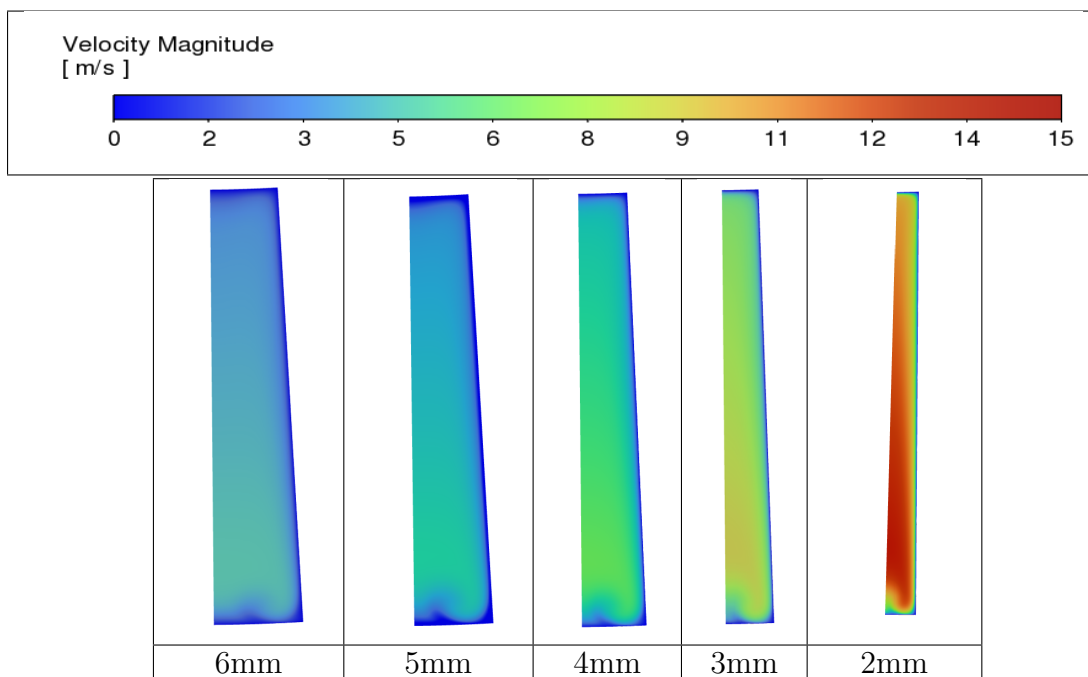
For the 2mm, 30-channel case, flow velocity was analytically calculated using Equa-

tion 4.1, where $\dot{m}$ represents the mass flow rate per channel, and A denotes the local cross-sectional area. These results were then compared to simulation data on graph 4.2

$$v = \frac{\rho. \cdot A}{A.\dot{m}} \tag{4.1}$$

A discrepancy of up to 15% between analytical and simulated flow velocities is observed, particularly near the throat region where flow velocity is highest. This likely stems from the simulation's incorporation of boundary layer effects, which reduce the effective flow area and consequently increase velocity. This analysis is crucial because velocity appears to be the pivotal variable influencing both pressure and, significantly, temperatures. This creates a delicate balance in heat transfer capabilities, ultimately playing a major role in mitigating wall temperatures.
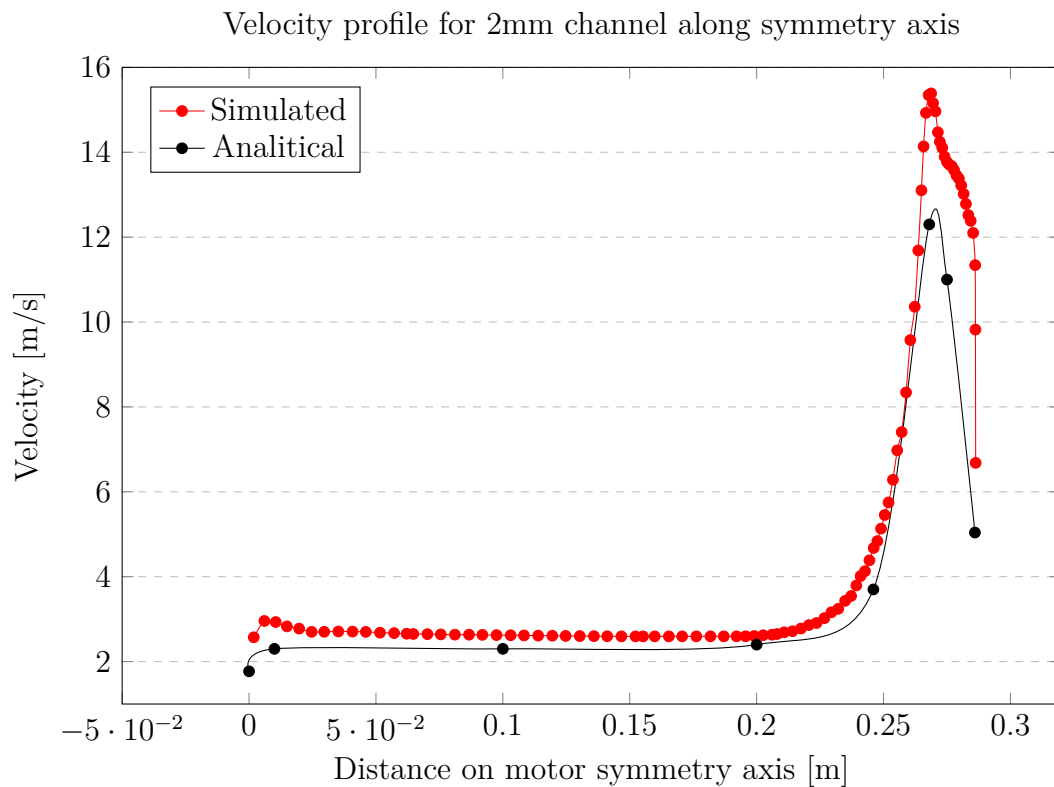
Figura 39 – Velocity profile for 2mm, 30 channels case along symmetry axis (Author)

The formation of a boundary layer was observed in both the outlet and throat regions, as illustrated in Tables 38 and 4.1. The layer's thickness exhibited an inverse relationship with flow velocity, minimized in the high-velocity throat region and maximized in the lower-velocity outlet region. This finding is significant as a boundary layer impedes heat transfer by hindering the efficient exchange of energy between the solid surface and the fluid.

However, the inherent surface roughness of 3D-printed components, characterized by its small-scale spatial variations and modeled as sand grain roughness in Ansys Fluent,

mitigates this detrimental effect. The roughness promotes turbulent mixing, reducing the boundary layer thickness and enhancing overall heat transfer performance. Figure 40 displays the boundary layer through the diverging converging nozzle in detail.
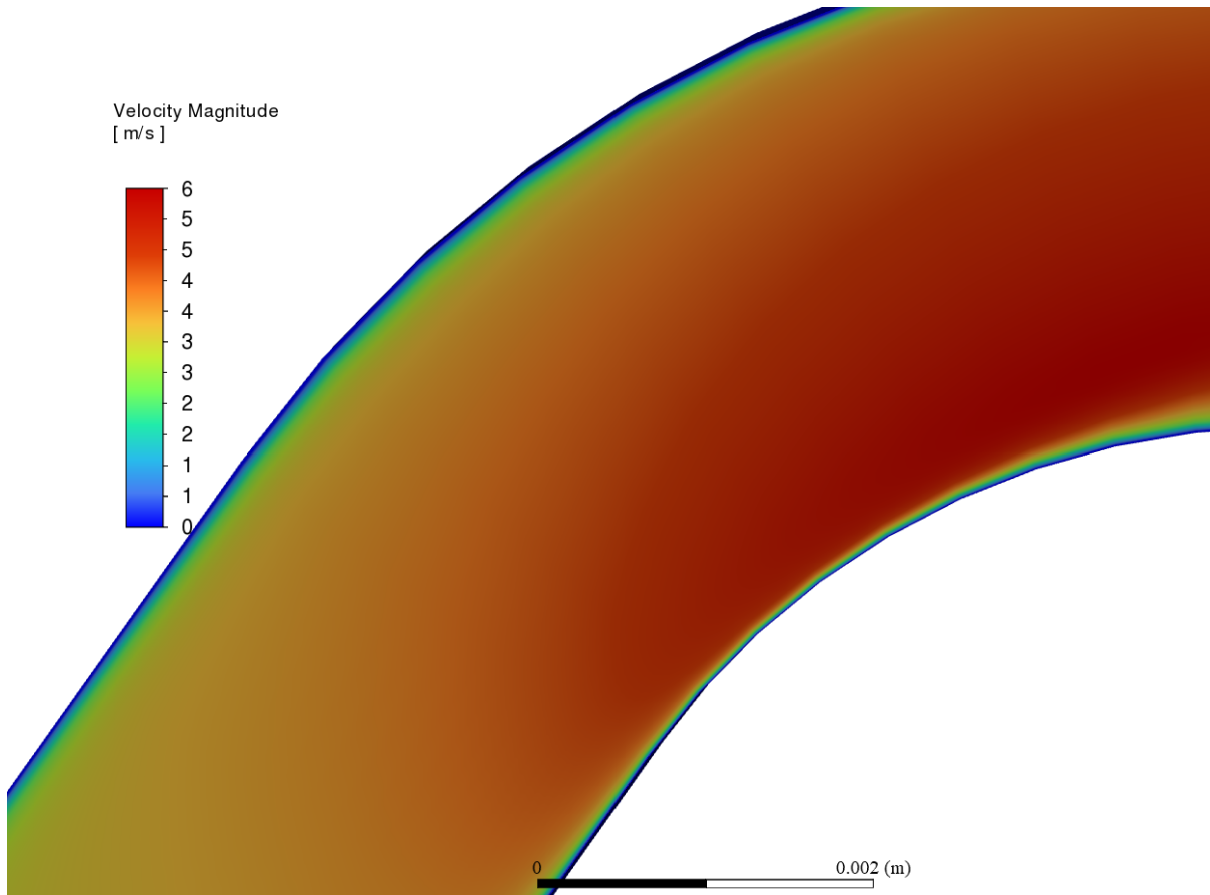
Figura 40 – Boundary layer visualization at nozzle region (Author)

However, the relationship between channel size, pressure, and velocity drop is not consistently linear. As illustrated in Graph 41, the pressure drop exhibits diminishing increases with increasing channel size. In contrast, the velocity increase is approximately linear.

In addition to the velocity profile, the pressure drop along the motor can be seen in table 43 the pressure drops only near the throat region, where the sectional area is significantly reduced, this can be seen on figure table 43.

Figura 41 – Velocity and pressure drop increase percentage when compared to 2mm results

Figura 42 – Velocity profile along nozzle extension for all 5 cases (Author)

Figura 43 – Pressure drop along nozzle extension for all 5 cases (Author)
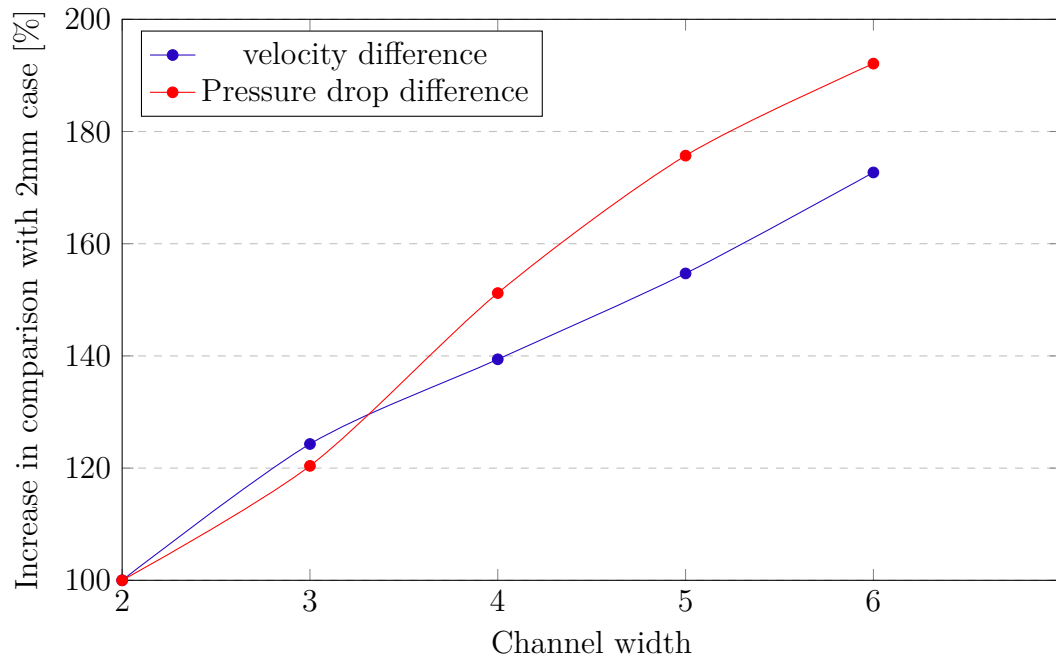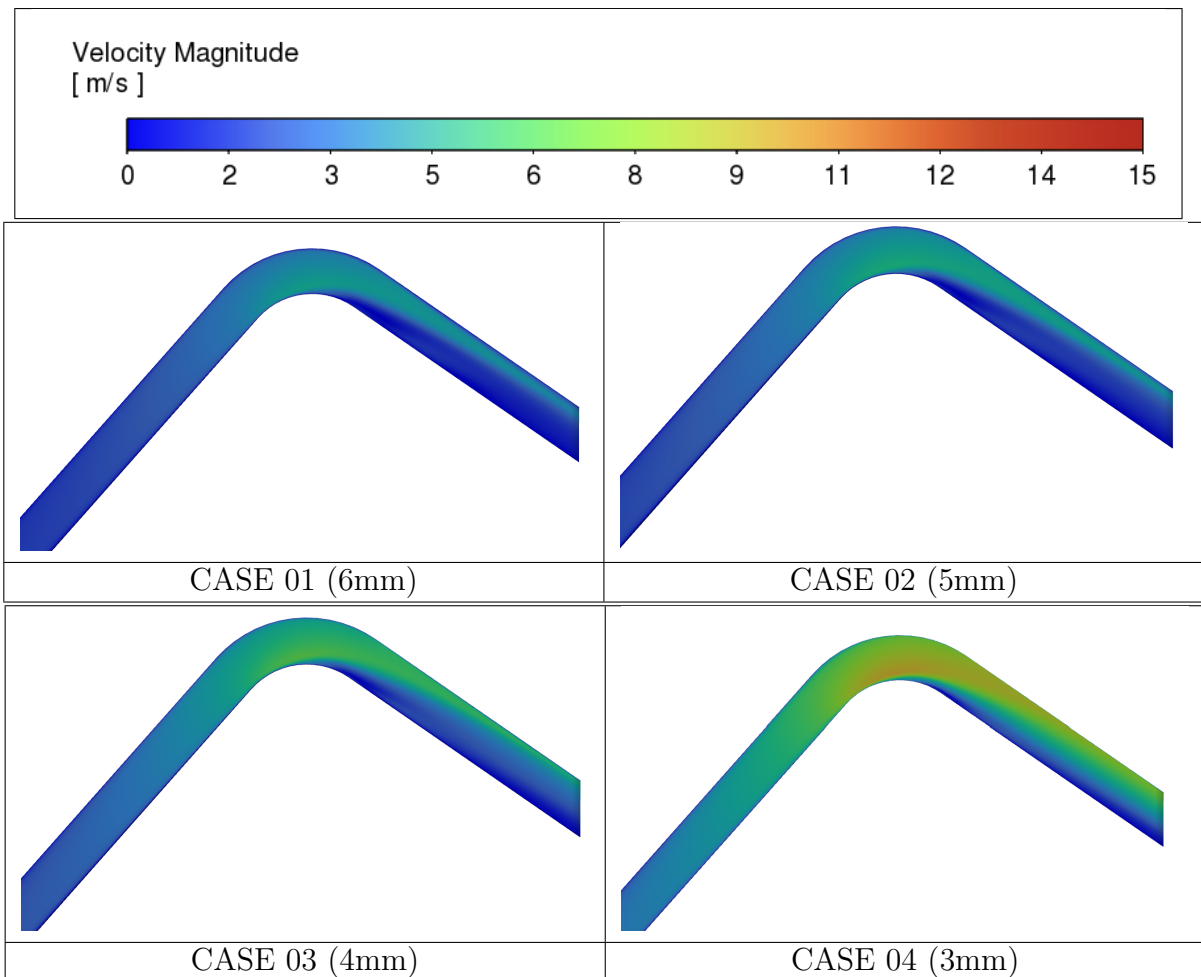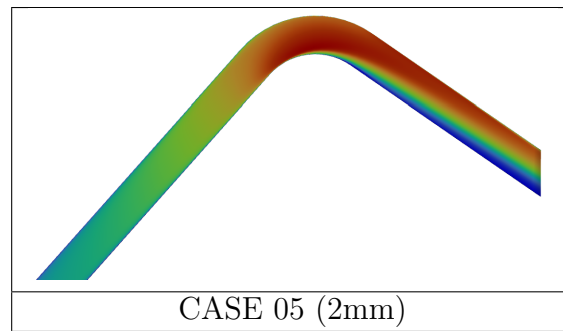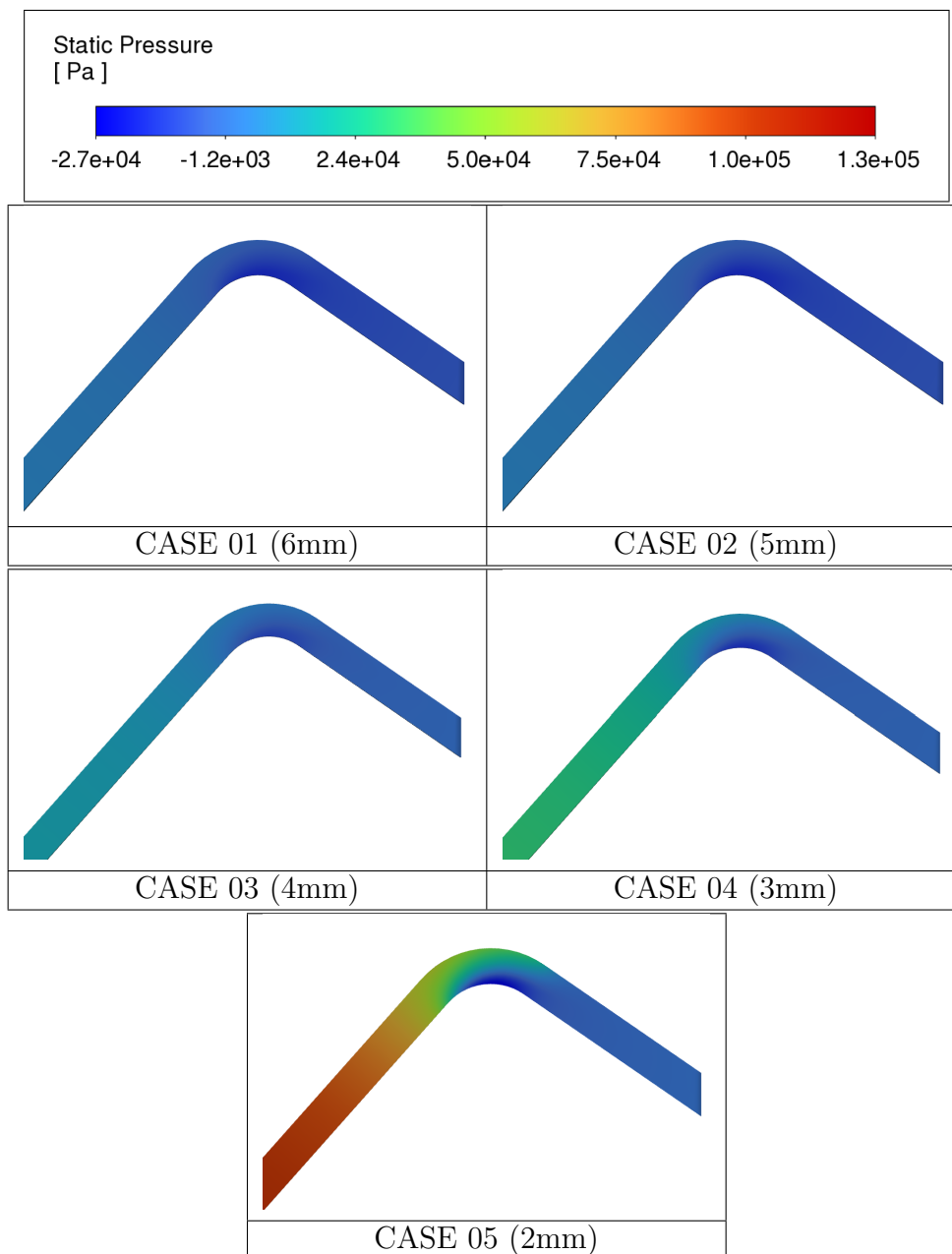
Excessive pressure drop in the cooling channels poses a critical risk in regenerative cooling systems, where the coolant flow is integral to the combustion process. If the coolant pressure falls below the chamber pressure, combustion stability is compromised, potentially leading to engine failure. This risk is particularly pronounced in high aspect ratio channels with minimal thickness. However, this concern is mitigated as the water coolant serves solely a thermal management function and does not directly influence the combustion process.

The primary goal of regenerative cooling is to mitigate thermal stresses on the combustion chamber walls, thereby extending both the duration of individual burns and the operational lifespan of the engine. To assess the efficacy of this cooling strategy, an analysis of the temperature distribution on the inner chamber wall is essential, particularly in the throat region, which experiences the highest thermal loading.

As detailed in Table 8, a reduction in the cooling channel width correlates with a decrease in the maximum temperature observed on the inner wall. This trend is visually represented in Graph 44, where the 6mm channel exhibits a maximum temperature of 942K, while the 2mm channel remains below 904.1K.
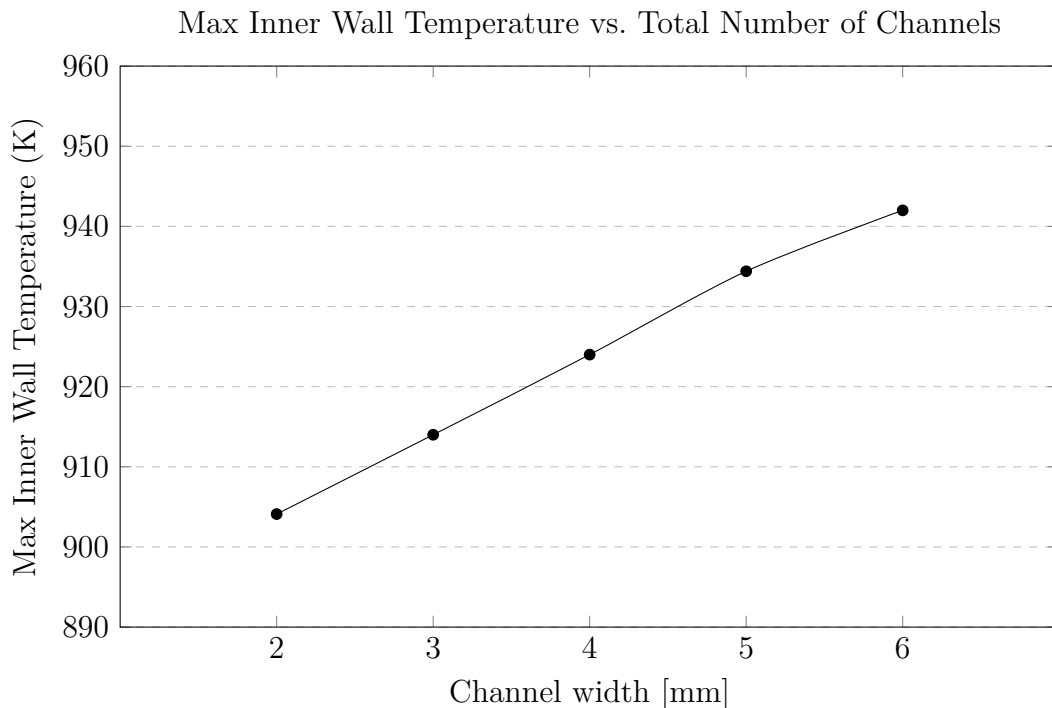
Figura 44 – Max Inner Wall Temperature vs. Channel width

A comprehensive visualization of the temperature gradient across the inner wall for the 2mm channel case is presented in Image 4.1. The observed temperatures remain well below the melting point of Inconel, indicating a safe operating margin for extended burn durations.
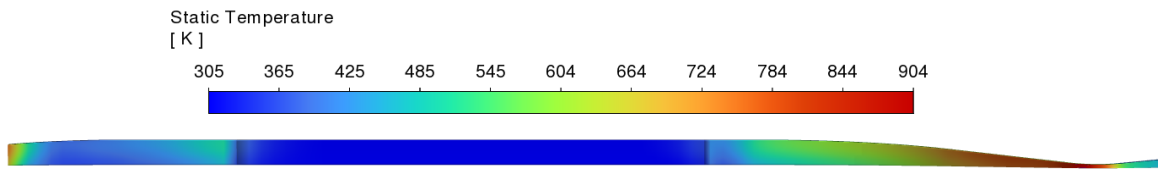
Figura 45 – Temperature profile 2mm case(Author)

Additionally, Graph 4.1 illustrates the temperature distribution along the motor axis, revealing a distinct peak in the throat region and notably cooler temperatures beneath the paraffin grain.

The cumulative evidence underscores the efficacy of regenerative cooling in preserving the structural integrity of the combustion chamber, thereby enhancing the engine's operational resilience and extending its lifespan.
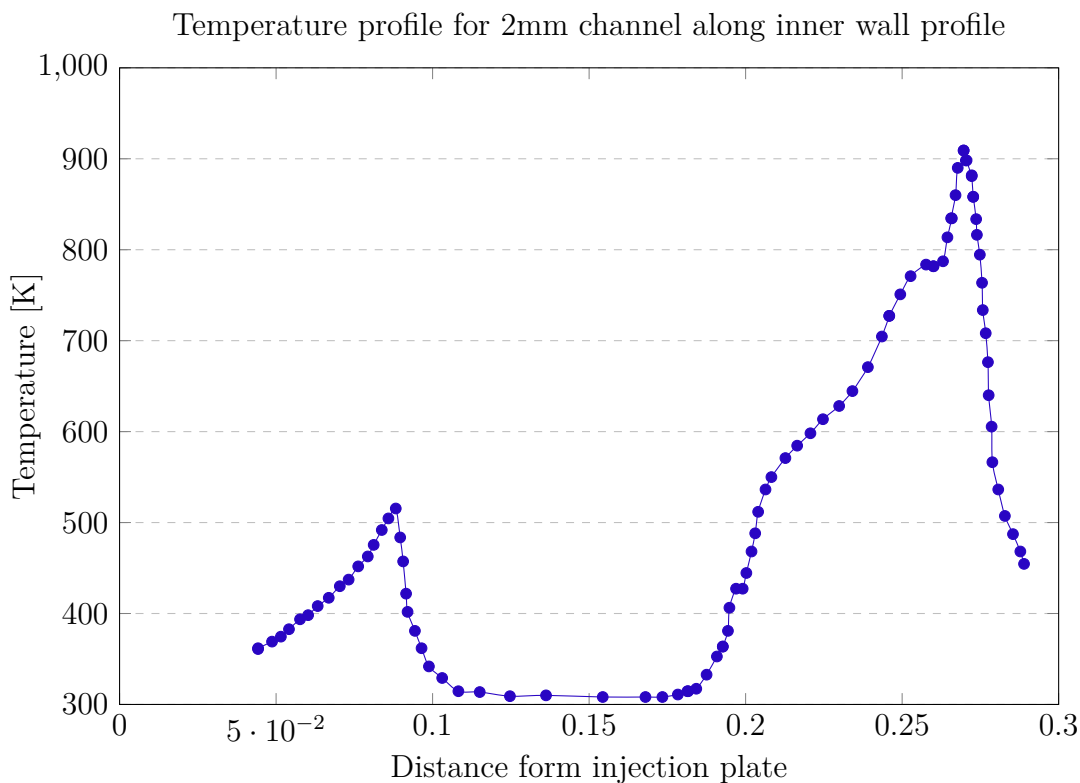
Figura 46 – Temperature profile for 2mm channel along inner wall profile (Author)

The observed data trends align with established literature, particularly the work by (ULAS; BOYSAN, 2013), thus validating the quality of the results obtained in this study. Based on its overall performance, characterized by lower inner wall temperatures despite a higher pressure drop, a 2mm channel width was selected for further simulations.

4.2   Results for number of channels

Utilizing the standardized 2mm channel width established in prior simulations, an investigation into the influence of the total number of cooling channels was conducted. Five distinct configurations were evaluated, as detailed in Table 9, encompassing variations in mass flow rates. Due to the accompanying changes in the chamber's cross-sectional area, the mass flow per channel was adjusted to maintain a constant total mass flow of 0.37 kg/s throughout the motor.

All other input parameters, including temperatures and pressures, were consistent with previous simulations, with a water inlet temperature of 300K and a combustion product inlet temperature of 1710K.

Tabela 9 – Parameters for number of channel configuration (Author)

	3 x 2 x 15	3 x 2 x 30	3 x 2 x 45	3 x 2 x 60	3 x 2 x 75
Channel height [mm]	3	3	3	3	3
Channel width [mm]	2	2	2	2	2
number of cooling channels	15	30	45	60	75
motor cross-section [degrees]	12	6	4	3	2.4
$\dot{m}$ (per channel) [kg/s]	0.0246	0.0123	0.0082	0.0061	0.0049

The flow characteristics within the combustion chamber, including temperature, Mach number, and pressure distributions, closely resemble those observed in Figures 35, 36, and 35 from the previous section.

Regarding overall performance, as presented in Table 10, a clear trend emerges indicating that a greater number of cooling channels does not necessarily translate to improved cooling efficiency.

Tabela 10 – Number of channels results (Author)

	3 x m x 15	3 x 2 x 30	3 x 2 x 45	3 x 2 x 60	3 x 2 x 75
motor cross-section [degrees]	12	6	4	3	2.4
number of cooling channels	15	30	45	60	75
Max inner wall temperature [K]	949.11	904.1	896.4	894.5	900.2
Max water temperature [K]	533.7	554.4	570.4	585.8	611
Average water temperature [K]	306.6	307.3	308.1	308.8	310
Pressure drop [bar]	4.37	1.23	0,61	0,37	0,26
Max water velocity [m/s]	30.1	15.4	10.6	8.1	6.58

The maximum water temperature, as anticipated, occurs near the throat region and exhibits an increasing trend with a greater number of channels. This suggests that the water absorbs more heat as the proportion of channels to wall area increases (Figure 47). The relationship between temperature increase and channel count is approximately linear, as illustrated by the trend line in Figure 48.
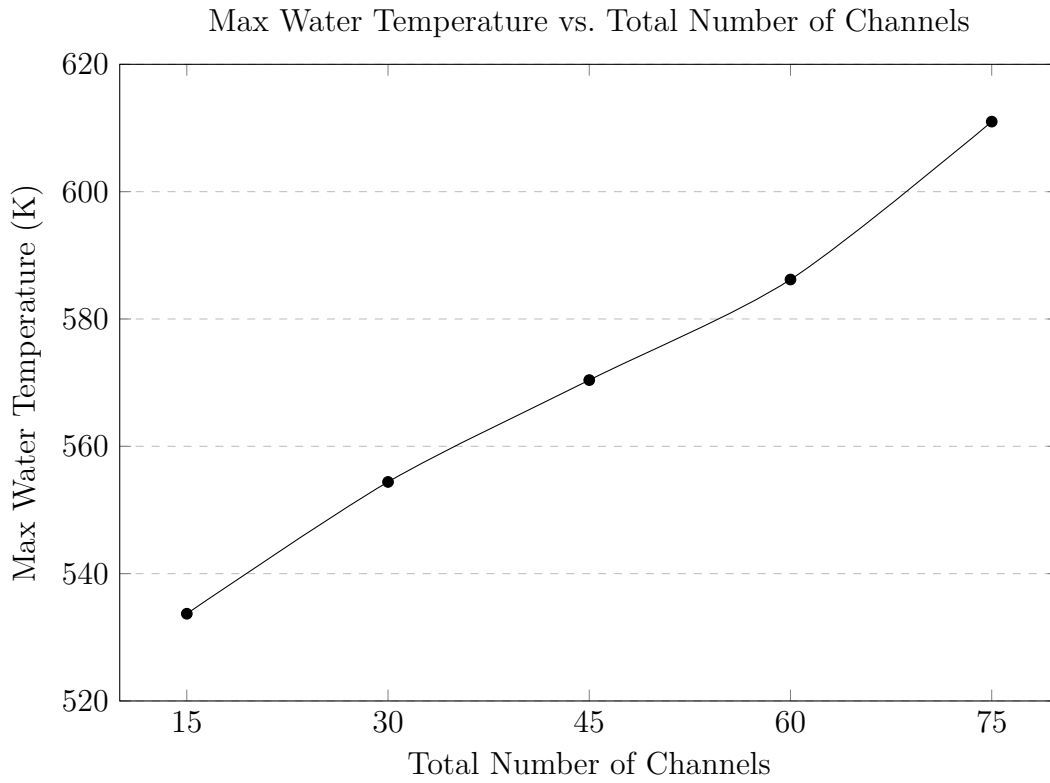
Max Water Temperature vs. Total Number of Channels

Figura 47 – Max Water Temperature vs. Total Number of Channels

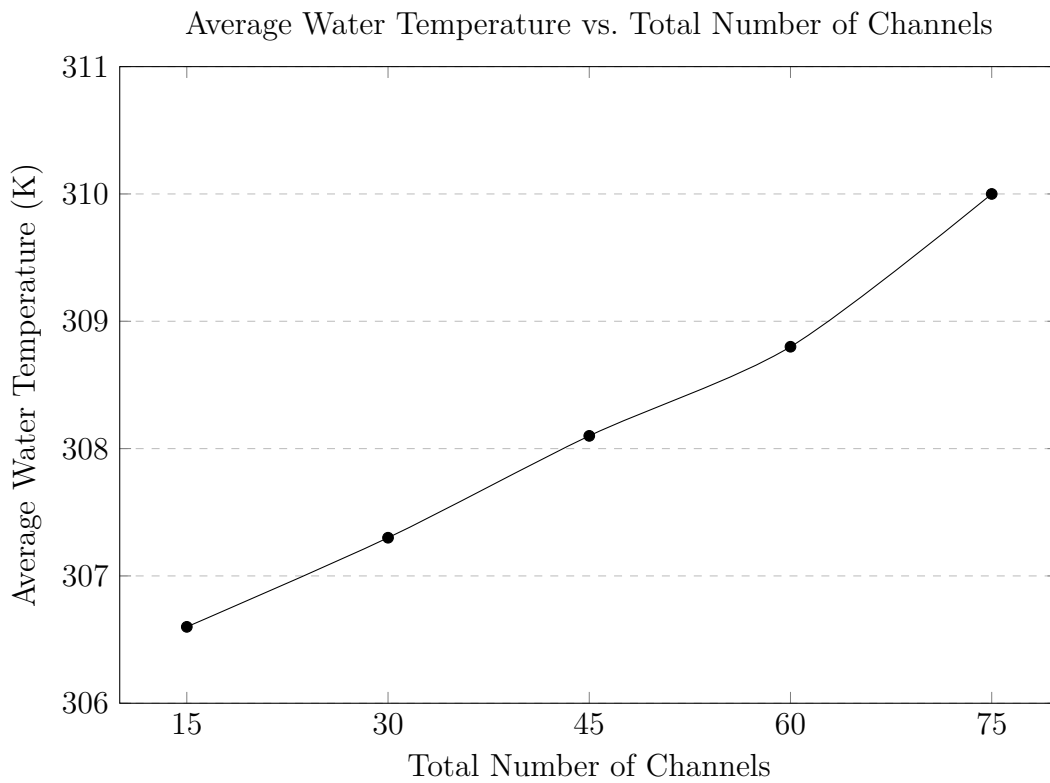Average Water Temperature vs. Total Number of Channels

Figura 48 – Average Water Temperature vs. Total Number of Channels

A substantial difference between the maximum and mean water temperatures indicates a highly localized temperature peak in the throat region. This localization, combined with the limited surface area, constrains the overall heat absorption capacity of the water.

Additionally, simulation results reveal that the water temperature approaches its boiling point near the boundary layer. This proximity to phase change suggests a potential for enhanced cooling efficiency due to the high latent heat associated with water vaporization. However, the current model does not incorporate phase change phenomena, therefore, this potential enhancement is not reflected in the present analysis.

However, unlike the linear correlation between water temperature and inner wall temperatures observed in the channel width analysis, the relationship between higher water temperatures and lower inner wall temperatures is not directly proportional in the case of varying channel numbers (Graph 49). Instead, the inner wall temperature reaches a minimum at 60 channels, indicating an optimal number of channels beyond which further increases do not necessarily improve cooling efficiency. This observation is consistent with the findings of Ulas et al. (2013), where a more pronounced minimum was observed.
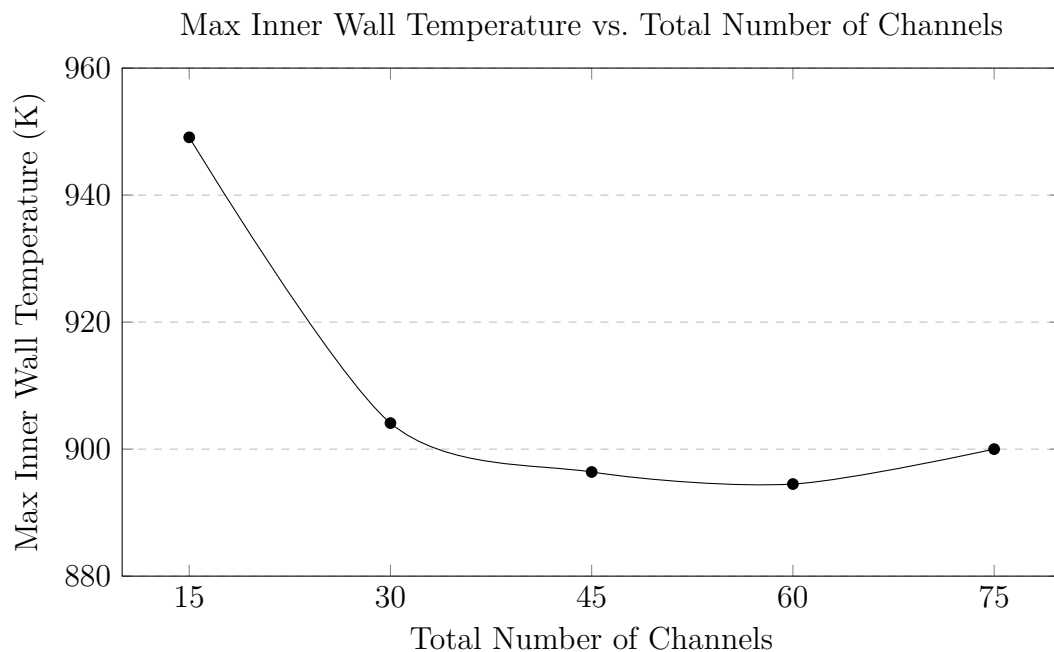
Figura 49 – Max Inner Wall Temperature vs. number of channels

The absence of a more distinct optimal value for channel count in the present work may be attributed to the motor's small size, which restricts the implementation of many channels on the scale seen in larger liquid rocket engines (100 to 300 channels). Additionally, the relatively low flow rate of the motor could diminish the overall effectiveness of regenerative cooling, rendering differences between geometries less pronounced.

Pressure drop exhibits an inverse logarithmic relationship with the number of channels 50, reaching over 4 bar for the highest channel count, meanwhile, the Max and

medium velocities follow the same logarithmic trend dropping more significantly on the 15 and 30 channel cases 51.

Pressure Drop vs. Total Number of Channels

Figura 50 – Pressure Drop vs. Total Number of Channels

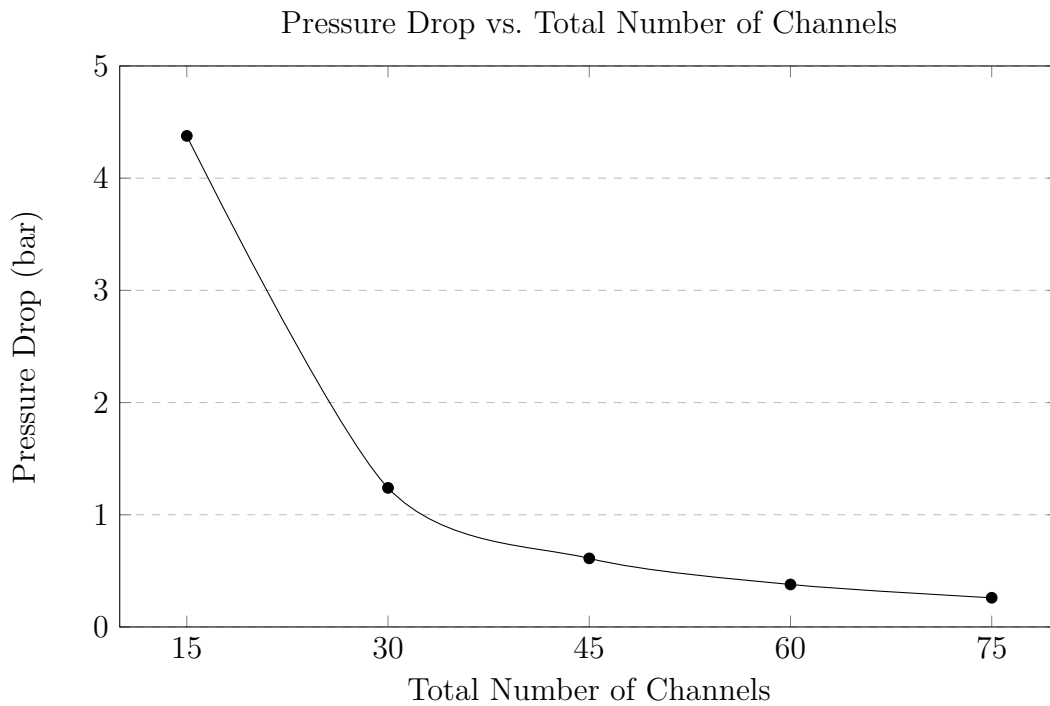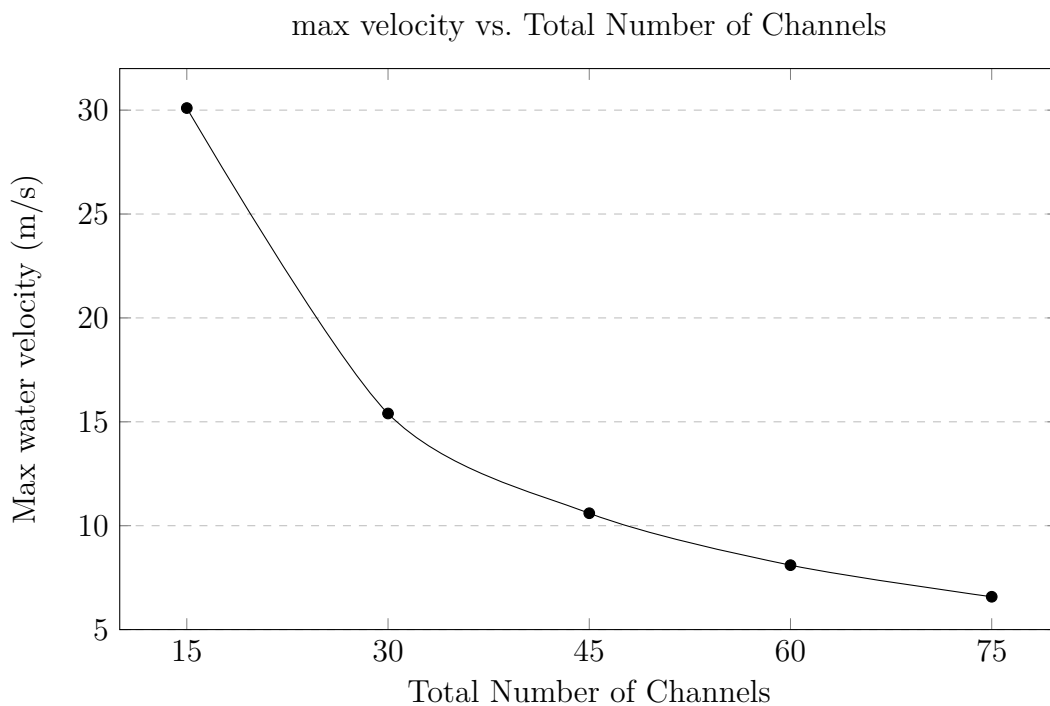max velocity vs. Total Number of Channels

Figura 51 – Max water velocity vs. Total Number of Channels

The optimal performance is achieved among the analyzed configurations with 2mm wide channels and 60 channel units. This configuration yields the lowest overall tempera-

tures among the tested cases, as illustrated in the temperature contour plot (Figure 53) and the temperature profile along the wall (Figure 4.2).
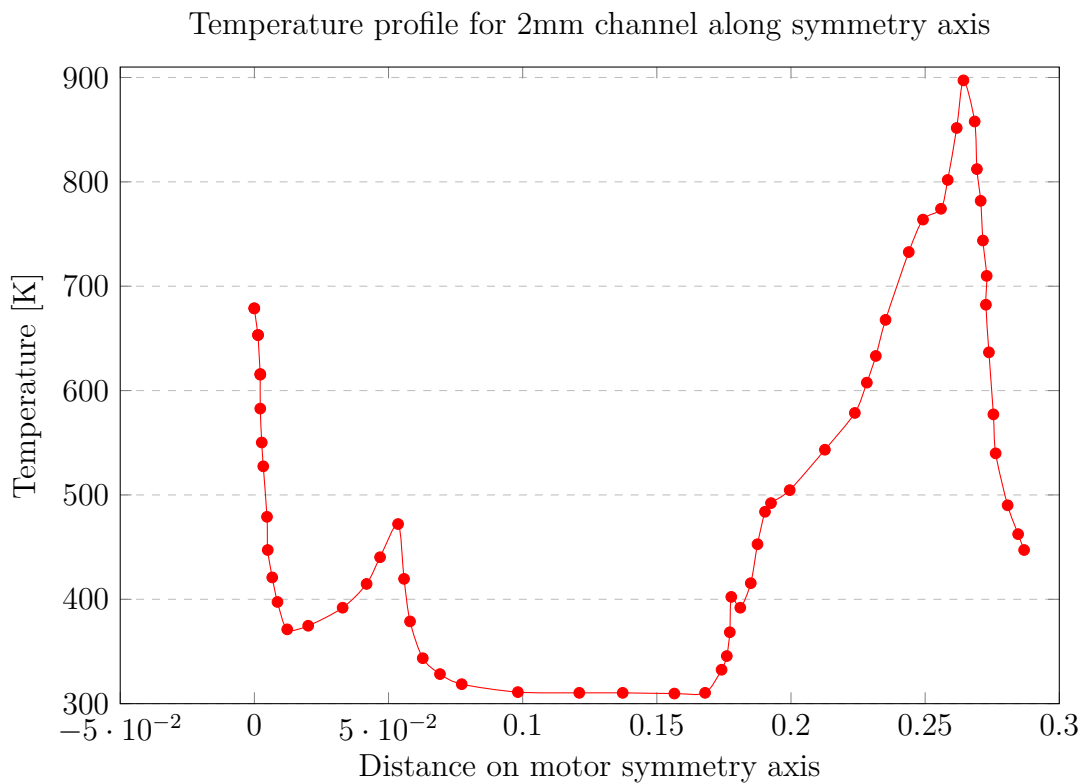
Figura 52 – Temperature profile for 2mm channel along symmetry axis (Author)
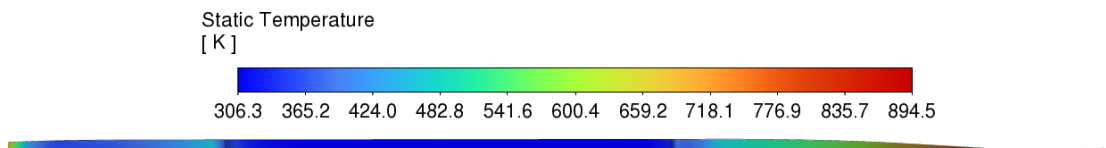
Figura 53 – Grapic Visualization of inner wall temperature contour for final optimized configuration (Author)

The velocity and pressure profiles for the water coolant within the 2mm and 60 channel configuration are presented in Graph 4.2 and Graph 4.2, respectively. These profiles demonstrate the impact of the throat region on the water flow parameters. The velocity of the coolant increases significantly as it passes through the throat region, while the pressure concurrently decreases. This behavior is characteristic of incompressible flow within a constricted passage.

Specifically, the acceleration of the coolant through the converging section leading to the throat results in a rise in velocity, accompanied by a drop in pressure. Beyond the throat, in the diverging section, the velocity decreases as the flow area increases, and the

Velocity for 2mm channel and 60 channels

Figura 54 – Velocity for 2mm channel and 60 channels (Author)

Static Pressure for 2mm and 60 channels configuration
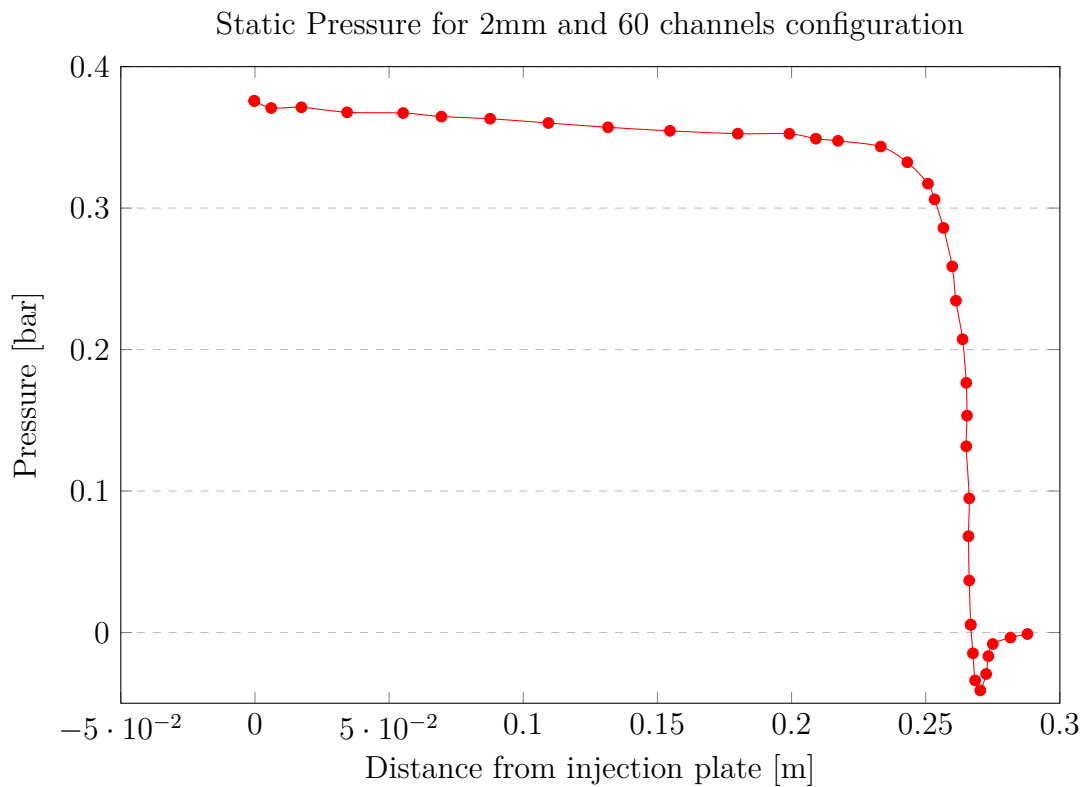
Figura 55 – Static Pressure for 2mm and 60 channels configuration (Author)

pressure slightly recovers. This pressure drop, while characteristic of fluid flow behavior, is carefully managed in the design to ensure sufficient coolant pressure for effective heat transfer and to avoid any risk of cavitation.
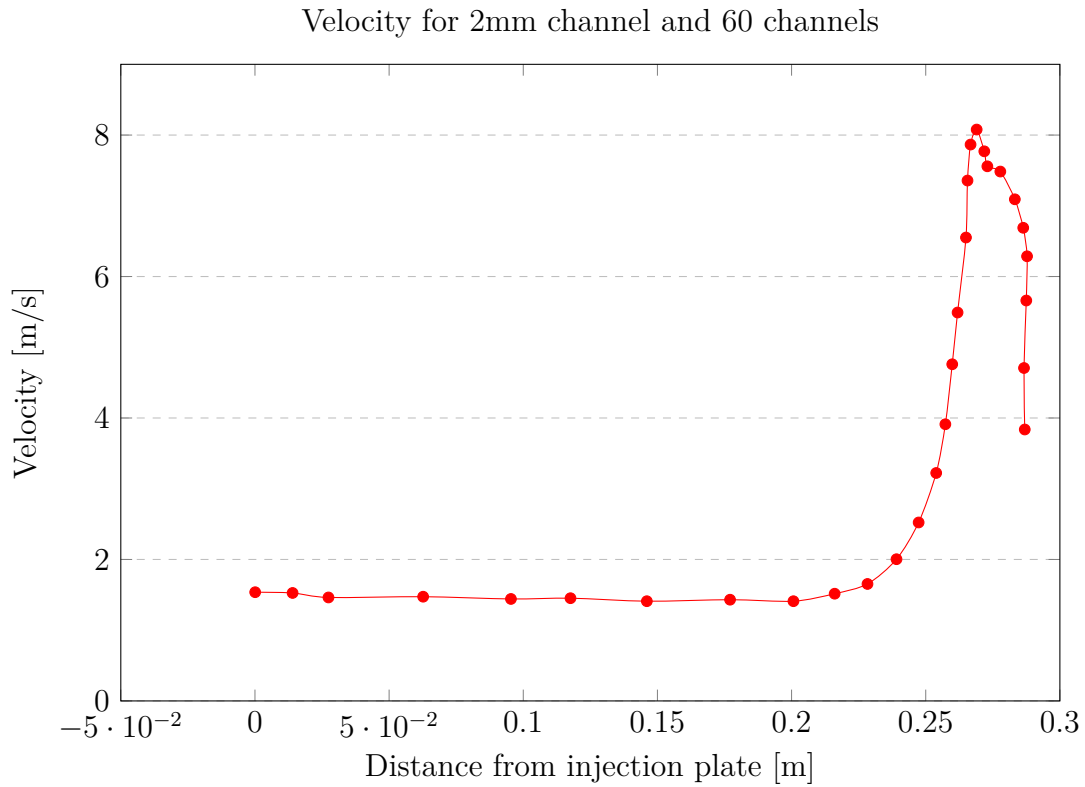
Figure 56 reveals flow detachment of the water from the outer channel wall, particularly near the throat region. This detachment, likely induced by the momentum change as the water accelerates through the nozzle, appears to recover as the flow moves downstream partially. However, due to the compact nozzle dimensions, full flow reattachment may not be achieved.
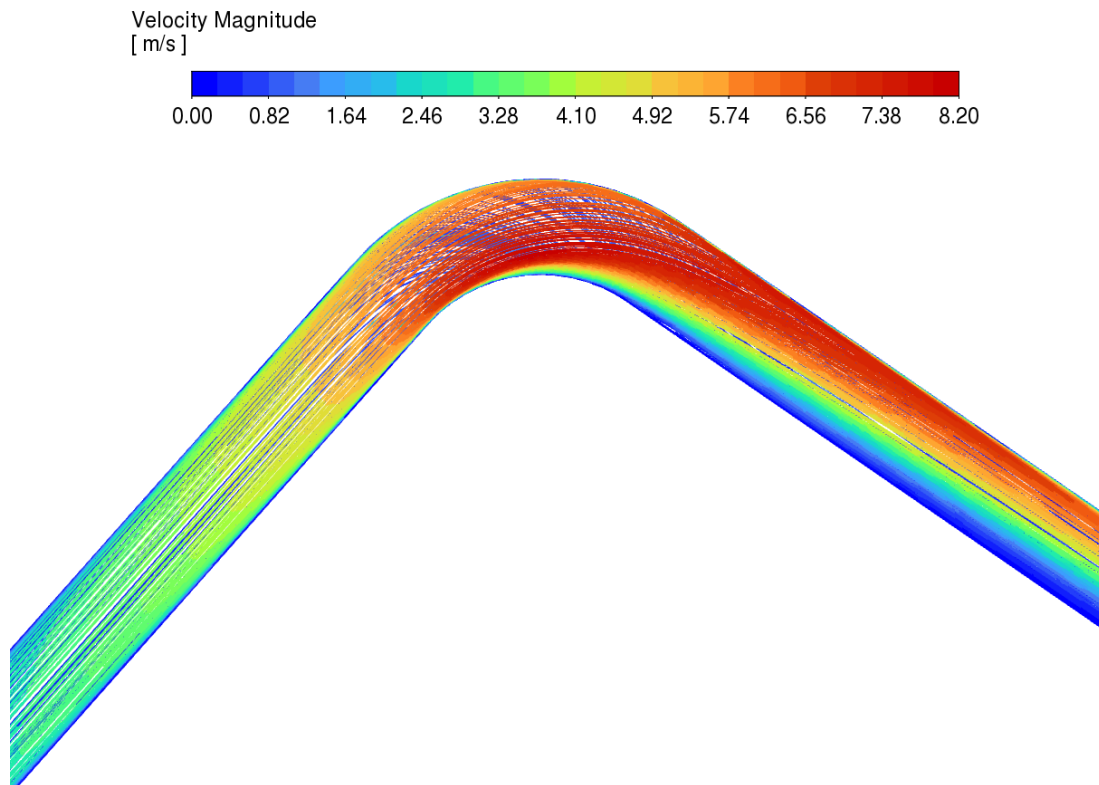
Figura 56 – Pathlines colored as velocity for nozzle region for 2mm 60 channel case (Author)

Furthermore, the path lines illustrated in Figure 57 and 58 exhibit a twisting pattern downstream of the grain region. As Palateerdham (2020) suggested, this phenomenon could be attributed to the thermal gradient within the channel and further amplified by the geometric variation as the channel cross-section narrows.

Figura 57 – Pathlines colored as velocity for nozzle region for 2mm 60 channel case (Author)

Figura 58 – Pathlines colored as velocity for nozzle region for 2mm 60 channel case (Author)

5 Final remarks
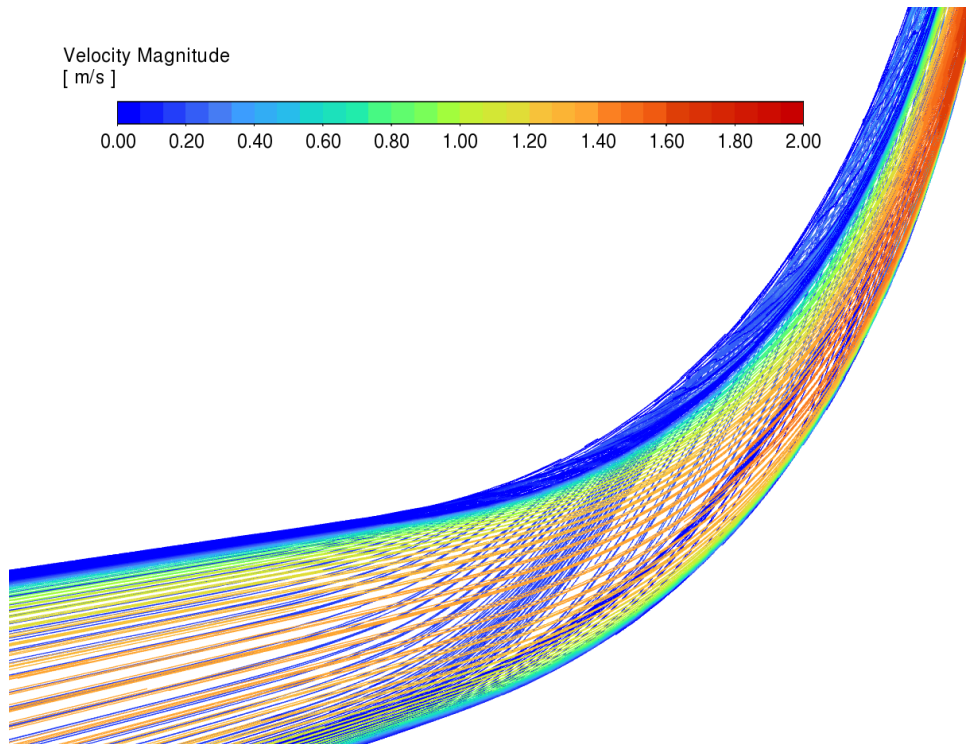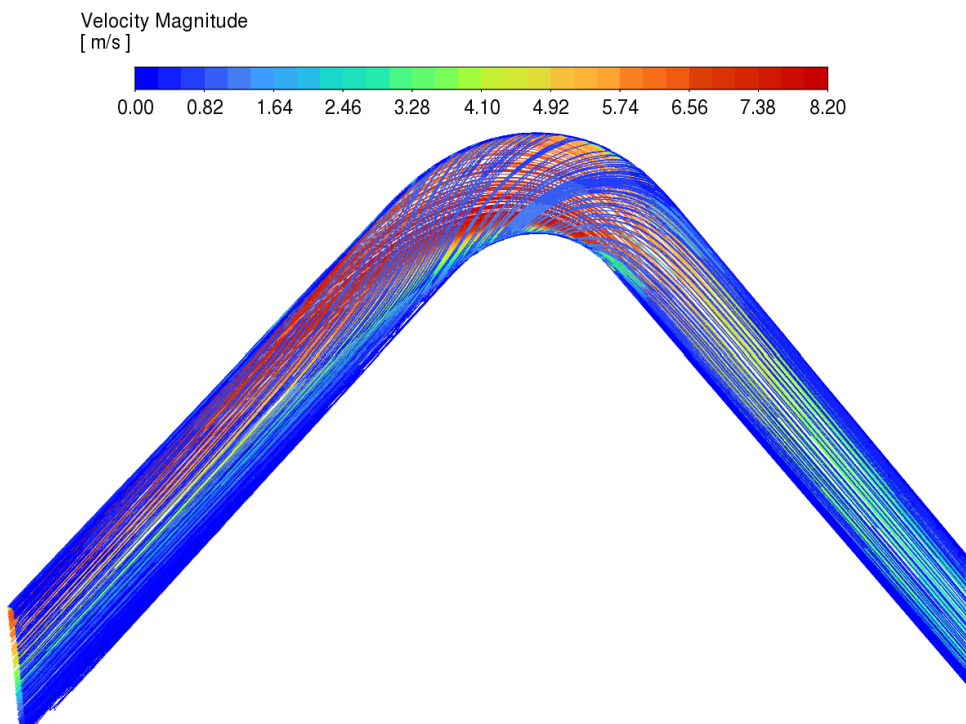
The primary objective of this work was to establish a robust theoretical foundation and conduct a preliminary simulation on the regenerative cooling design of an additive manufacturing (AM) motor. This aimed to prove the concept and achieve adequate cooling of the SARA v3 engine during extended burn durations, a critical requirement for ensuring engine performance and longevity.

During the study, ten different motor configurations were considered. These included five different channel widths, and the most efficient width was then selected for evaluating five different numbers of channel configurations. This comprehensive approach was crucial for understanding the interaction between channel width and the number of channels on the overall cooling performance of the motor.

The findings indicate that wall temperatures also decrease as the channel width decreases. However, this trend converges to the point of maximum performance as the size gets smaller. Additionally, the decrease in heat transfer is accompanied by significant increases in pressure drop and flow velocity within the cooling channels. This relationship underscores the need for a balanced design that optimizes thermal performance without incurring excessive pressure drops. In regenerative cooling engines, excessive pressure drops can be very detrimental as they reduce the cooling system's efficiency, leading to inadequate cooling and potential overheating of the engine. However, this is less critical since we are not using actual regenerative cooling but rather water, which simplifies the cooling requirements.

Smaller channels yield better thermal performance but require more refined printing techniques. To mitigate this requirement, variable cross-sectional area (VCSA) designs may need to be incorporated. VCSA designs can reduce the necessary printing resolution, especially in the throat region where sizes are minimal. This approach balances optimal performance and more forgiving manufacturing tolerances, making it a practical solution for the real-world application of AM motors.

Regarding the number of channels, the relationship between wall temperatures and the number of channels displays a valley, indicating an optimum number of channels. This optimal number can vary based on the size and mass flow of the motor, along with other variables not considered in this work. The results contrast with the second-order curve observed in the number of channel analyses, where pressure drop and water temperatures (both average and maximum) followed a linear increase. This suggests that higher water temperatures, which should indicate better heat absorption and, consequently, lower wall temperatures, do not directly translate to better performance.

The simulations also indicate that the motor is too small and has too little surface area to heat the water and effectively transfer large amounts of heat. This is due to the cubic relationship between the area and the motor's radius. The motor's mass flow rate is also relatively small (0.37 kg/s), limiting its cooling capabilities. This results in only about 10 K of water heating at maximum cooling performance. The maximum water temperatures are much higher but occur only at the throat region, a very small point due to boundary layer formation, and do not translate to significantly higher average temperatures. This limitation highlights the challenges faced when designing small-scale regenerative cooling systems.

The best cooling performance was found with 2mm width channels and 60 total channels, as shown in Table 11. This configuration provided a balanced solution with optimal thermal performance and manageable pressure drops, demonstrating the importance of selecting appropriate channel dimensions.

Tabela 11 – Best performing cooling configuration (Author)

	3 x 2 x 60
Motor cross-section [degrees]	3
Number of cooling channels	60
Max inner wall temperature [K]	894.5
Max water temperature [K]	585.8
Average water temperature [K]	308.8
Pressure drop [bar]	0.37
Max water velocity [m/s]	8.1

For future work, configurations considering variations in channel height should be explored. This is particularly relevant because other studies, such as (ULAS; BOYSAN, 2013), achieved better results with higher aspect ratio channels. Additionally, a detailed VCSA analysis is needed to facilitate the production process and enable the real-life printing of the SARA v3 motor. Such an analysis would help balance manufacturing capabilities with performance requirements, ensuring that the motor can be produced efficiently while meeting the stringent cooling demands of extended burn durations. Furthermore, investigating alternative cooling fluids and enhanced heat transfer techniques could provide additional insights and improvements for future designs.

Referências

AMFG. *Application spotlight: 3D-printed rockets and the future of space-craft manufacturing.* 2020. Disponível em: <https://amfg.ai/2019/08/28/application-spotlight-3d-printed-rockets-and-the-future-of-spacecraft-manufacturing/>. Citado 2 vezes nas páginas 11 e 30.

ANDERSON, J. D. *Computational Fluid Dynamics: The basics with applications.* [S.l.]: McGraw-Hill, 2010. Citado 2 vezes nas páginas 42 e 54.

ANDERSON, J. D. *Fundamentals of aerodynamics.* [S.l.]: McGraw-Hill, 2011. Citado 6 vezes nas páginas 11, 40, 41, 42, 44 e 55.

ANSYS, I. *ANSYS FLUENT Theory Guide.* [S.l.]: ANSYS, Inc., 2011. Citado 5 vezes nas páginas 42, 43, 54, 60 e 61.

BLAKEY-MILNER, B. et al. Metal additive manufacturing in aerospace: A review. *Materials Design*, v. 209, p. 110008, 2021. ISSN 0264-1275. Disponível em: <https://www.sciencedirect.com/science/article/pii/S0264127521005633>. Citado 3 vezes nas páginas 11, 33 e 34.

BOYER, R.; FROES, F. H. *Additive Manufacturing for the aerospace industry.* [S.l.]: Elsevier, 2019. Citado na página 30.

BROWNE, E. C. *MODELING ABLATIVE AND REGENERATIVE COOLING SYSTEMS FOR AN ETHYLENE/ETHANE/NITROUS OXIDE LIQUID FUEL ROCKET ENGINE.* Tese (Doutorado), 2020. Citado na página 32.

BUSSMANN, A. Parametric study on hybrid rocket propulsion system performance measured by the system specific impulse. 2022. Citado 2 vezes nas páginas 11 e 27.

FRAZIER, W. E. Metal additive manufacturing: A review. *Journal of Materials Engineering and Performance*, v. 23, n. 6, p. 1917–1928, 2014. Citado 2 vezes nas páginas 29 e 53.

GRADL, P. R.; PROTZ, C. S. Technology advancements for channel wall nozzle manufacturing in liquid rocket engines. *Acta Astronautica*, v. 174, p. 148–158, 2020. Citado 2 vezes nas páginas 11 e 34.

KESTIN, J. et al. Thermophysical properties of fluid h2o. *Journal of Physical and Chemical Reference Data*, v. 13, n. 1, p. 175–183, 1984. Citado 3 vezes nas páginas 15, 53 e 55.

KOTHANDARAMAN, C. P. *Fundamentals of heat and mass transfer.* [S.l.]: New Age International (P) Limited, Publishers, 2012. Citado 6 vezes nas páginas 11, 36, 37, 38, 39 e 40.

KUO, K. K.; CHIAVERINI, M. J. *Overview and History of Hybrid Rocket Propulsion.* [S.l.]: American Institute of Aeronautics and Astronautics, 2007. 1-36 p. Citado 2 vezes nas páginas 27 e 28.

MENTER, F. R. Influence of freestream values on k-omega turbulence model predictions. *AIAA Journal*, v. 30, n. 6, p. 1657–1659, 1992. Citado 3 vezes nas páginas 11, 46 e 47.

PALATEERDHAM, S. Experimental investigation of the paraffin thermomechanical properties and hybrid rocket engine performance for different fuel grain formulations. 2020. Citado na página 32.

SALIM, S. M.; CHEAH, S. Wall y+ strategy for dealing with wall-bounded turbulent flows. *Int. MultiConf. Eng. Comput. Sci. (IMECS)*, v. 2, p. 1–6, 01 2009. Citado 3 vezes nas páginas 54, 55 e 57.

SHYNKARENKO, O. *SARA V3 rocket*. 2022. Citado 4 vezes nas páginas 11, 27, 29 e 50.

SING, S. et al. 3d printing of metals in rapid prototyping of biomaterials: Techniques in additive manufacturing. *Rapid Prototyping of Biomaterials*, p. 17–40, 2020. Citado 3 vezes nas páginas 11, 30 e 31.

SMOOT, J. *Monitoring, control, and protection options in DC fans for Air Cooling*. 2021. Disponível em: <https://www.edn.com/monitoring-control-and-protection-options-in-dc-fans-for-air-cooling/?_ga=2.61873132.1314086268.1699330180-1814848557.1699330180&_gl=1%2A9bvkwb%2A_ga%2AMTgxNDg0ODU1Ny4xNjk5MzMwMTgw%2A_ga_ZLV02RYCZ8%2AMTY5OTMzMDE4MC4xLjEuMTY5OTMzMDMyNC4zOC4wLjA.> Citado 2 vezes nas páginas 11 e 38.

SOUSA, F. S. *Simulação de Escoamentos multifásicos em malhas Não Estruturadas*, 2005. Citado na página 54.

SPALDING, B. Kolmogorov's two-equation model of turbulence. *Proceedings of the Royal Society of London. Series A: Mathematical and Physical Sciences*, v. 434, n. 1890, p. 211–216, 1991. Citado na página 46.

SUTTON, G. P.; BIBLARZ, O. *Rocket Propulsion Elements*. [S.l.]: John Wiley amp; Sons, Inc, 2017. Citado na página 23.

ULAS, A.; BOYSAN, E. Numerical analysis of regenerative cooling in liquid propellant rocket engines. *Aerospace Science and Technology*, v. 24, n. 1, p. 187–197, 2013. ISSN 1270-9638. VFE-2. Disponível em: <https://www.sciencedirect.com/science/article/pii/S127096381100191X>. Citado 8 vezes nas páginas 11, 35, 36, 49, 53, 67, 74 e 84.

VEKILOV, S. S.; LIPOVSKYI, V.; MARCHAN, R. A. Features of the adaptation of 3d printed regenerative cooling channels of the lpre throat inserts. *System design and analysis of aerospace technique characteristics*, v. 29, n. 2, p. 62–72, 2021. Citado 4 vezes nas páginas 11, 23, 33 e 34.

VERSTEEG, H. K.; MALALASEKERA, W. *An introduction to computational fluid dynamics: The Finite Volume Method*. [S.l.]: Prentice Hall, 2011. Citado na página 49.

WIBERG, A. *Towards design automation for additive manufacturing: A multidisciplinary optimization approach*. [S.l.]: Linkopings Universitet, 2019. Citado 3 vezes nas páginas 11, 31 e 32.

WILCOX, D. C.; WILCOX, D. C. *Solutions manual turbulence modeling for CFD.* [S.l.]: DCW Industries, Inc., 2006.   Citado 2 vezes nas páginas 46 e 47.

ÇENGEL, Y. A.; GHAJAR, A. J. *Heat and mass transfer: Fundamentals amp; applications.* [S.l.]: McGraw-Hill Education, 2020.   Citado 2 vezes nas páginas 37 e 44.